Progress in Crystal Growth and Characterization of Materials 66 (2020) 100485

Contents lists available at ScienceDirect

Progress in Crystal Growth and Characterization of Materials

journal homepage: www.elsevier.com/locate/pcrysgrow

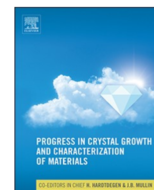

Review

Arsenides-and related III-V materials-based multilayered structures for terahertz applications: Various designs and growth technology

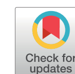

Alexander E. Yachmenev[a], Sergey S. Pushkarev[a], Rodion R. Reznik[b,c], Rustam A. Khabibullin[a,d], Dmitry S. Ponomarev[a,e,f,*]

[a] Institute of Ultra High Frequency Semiconductor Electronics of RAS, 117105 Moscow, Russian Federation
[b] Alferov University, 194021 St-Petersburg, Russian Federation
[c] Saint-Petersburg Scientific Center RAS, 199034 St. Petersburg, Russia
[d] Bauman Moscow State Technical University, Moscow 105005, Russian Federation
[e] Prokhorov General Physics Institute of the Russian Academy of Sciences, Moscow 119991, Russia
[f] Institute for Physics of Microstructures, Russian Academy of Sciences, Nizhny Novgorod 603950, Russia

ARTICLE INFO

Keywords:
Molecular-beam epitaxy
A3B5 semiconductors
Terahertz frequency range
Terahertz emitters and detectors
Superlattices
Binary and ternary compounds
InGaAs
GaAs
InAs
AlAs
Lattice-matched and strained layers
Quantum well
Terahertz radiation
Multilayered heterostructure
Pulse terahertz radiation
Continuous-wave terahertz radiation
Quantum cascade laser
Photoconductive materials
Photoconductive antenna
Low-temperature grown GaAs.

ABSTRACT

The fabrication and investigation of single and multilayered structures have become an essential issue in the past decades since these structures directly define valuable properties and efficiency of widely used terahertz (THz) emitters and detectors. Since the development of molecular-beam epitaxy, as well as other crystal growth techniques, a variety of structural designs has appeared and has been proposed. Since that, an enormous progress has been achieved beginning from the pioneering work on photoconductivity in silicon toward different multilayered heterostructures. The last are now commonly utilized as base components in photoconductive THz emitters/detectors, quantum-cascade lasers for pulsed and continuous-wave THz spectroscopic and imaging systems providing critical fundamental and practical applications at the forefront of scientific knowledge (sensors, flexible electronics, security systems, biomedicine, and others). This review summarizes the developments in different approaches and crystal growth techniques, emphasizing the importance of using single and multilayered arsenides-and related III-V materials-based (phosphides, antimonides, bismuthides) structures to accomplish the needs of modern and existing instruments of THz science and technology.

Introduction

Since the first observations of THz radiation [1,2] the THz range of electromagnetic spectrum attracts considerable attention due to the specificity of THz wave – matter interactions: the THz dielectric response contains information on low energy molecular vibrations and structural features of media [3]. This allows for using the THz spectroscopy and imaging for solving numerous fundamental and applied problems in condensed matter physics and material science [4–6], gas sensing [7], chemistry and pharmaceutical industry [8–10], security applications [11–13], biology and medicine [14,15].

The new THz era began with the pioneering Auston's research on photoconductivity in amorphous silicon and radiation-damaged silicon on sapphire [16] followed by fast-developing progress owing to discover of low-temperature grown GaAs (LT-GaAs). The LT-GaAs allows to generate and detect the THz waves thanks to its short photocarrier lifetime < 1 ps and high dark resistance) [17,18]. Along with ion-implanted GaAs [19,20] the LT-GaAs became the most commonly used photoconductive material for different THz spectroscopic systems that operate with 800 nm Ti:Sapphire laser wavelength. The second era started with $In_{0.53}Ga_{0.47}As$, which can efficiently operate with the telecom fiber lasers thanks to its narrow energy bandgap and allows

* Corresponding author at: Nagorniy proezd 7 (IUHFSE RAS),117105 Moscow, Russian Federation.
E-mail address: ponomarev_dmitr@mail.ru (D.S. Ponomarev).

https://doi.org/10.1016/j.pcrysgrow.2020.100485

Available online 14 April 2020
0960-8974/ © 2020 Elsevier Ltd. All rights reserved.

fabricating cost-effective and portable THz devices. Importantly, the aforementioned photoconductive structures for both wavelengths consisted of a bulk semiconductor layer, and the following advancement in THz researches, as well as a dead-end in the further improvement of single-layer structures like LT-GaAs, Be-doped InGaAs or ion-implanted GaAs and InGaAs, resulted in the necessity of new designs of the photoconductive structures. In the pioneering work [21], M. Koch et al. demonstrated that short-period GaAs/AlAs superlattices (SLs) exhibit ultrafast response when excited by the Ti: Sapphire laser manifesting in observation of photon echoes, which are the consequence of the inhomogeneous broadening of the excitonic resonance. Further, the employment of multilayered structures, mostly based on arsenides- and related III-V materials, revealed unprecedented design flexibility. For instance, by using additional functional layers like heat-spreading AlAs layer or distributed Bragg reflector (DBR) could either improve the performance of conventional photoconductive layers [17,22] or create fundamentally new structures as ErAs or InAs quantum dotted (QD) SLs [23,24]. The utilization of these approaches allows not only to achieve fast switching [23,25] or high-mobility [26–28] in photoconductive structures with required energy bandgap (depending on optical pump wavelength) but also utilize interband recombinations states [29,30], tune the intraband quantization levels [31,32], relaxation times and mobility [25,33,34], and others depending on assigned objectives. Importantly, that valuable THz devices such as quantum-cascade lasers (QCLs) or resonant-tunneling diodes (RTDs) are inherent multilayered.

The research on multilayer structures has provided a phenomenal increase in the efficiency and sensitivity of contemporary THz emitters and detectors. For instance, in [35], the authors demonstrated a 1.4 mW radiated THz power using a large-area emitter based on the ErAs/GaAs SLs, while in [27] it was reported of a 64 μW THz power from emitter based on high mobility InGaAs/InAlAs SLs (see Section I). The development of heterostructures demonstrating suppression in various scattering mechanisms led to a sufficient increase in the THz QCL operating temperatures from 50 K [36] to almost 211 K [37] (see Section II). The authors of [38] reported on a frequency above 1.9 THz, which was emitted by the RTD (see Section III).

Despite the impact of a multilayer design on the THz component base, most of the recent reviews have been dedicated predominantly to device optimization [39–42] or bulk semiconductor materials [43].

This paper is organized as follows.

In Section 1 we summarize recent developments in the area of semiconductor structures aimed at the enhancement of emission and detection of the THz waves via photoconductive antennas (PCAs), as well as the THz generation using *p-i-n* diodes. A brief comparison with conventional bulk semiconductor structures is given and recent studies that are focused on multilayer binary compounds with DBR and complex-designed SLs including lattice-matched and strained InGaAs/InAlAs structures, ErAs/GaAs and ErAs/Be:InGaAs layers, as well as InAs/GaAs QD structures, and some others.

In Section 2 we cover the aspects of multilayer structures for THz QCL growth and the approaches aimed at the modification of QCL's active region designs.

In Section 3 we consider heterostructures for the RTDs operating as THz emitters and the SL-based diodes that are mostly used as frequency multipliers to convert external GHz signal to the THz one.

1. Multilayered structures for photoconductive devices

In this section, we mainly consider multilayered structures, in which absorption of optical pulses leads to the appearance of photocarriers which, are driven by internal or external direct current (DC) electric field. The resultant time-dependent photocurrent is a convolution of the instantaneous laser intensity with respect to the concentration of photocarriers and their drift velocity. The considered structures are used in photoconductive devices (THz emitters and detectors) that operate at room temperature.

1.1. Structures for photoconductive antennae

1.1.1. Binary compounds

Amongst a variety of contemporary THz emitters and detectors, PCAs have become the prevalent ones. They are currently widely used as key elements in pulse and continuous-wave (CW) THz spectroscopic and imaging systems thanks to their reliability, cost-effectiveness, relative ease of fabrication, and flexibility of their design. Being used with femtosecond lasers, the PCAs exhibit a broad spectrum up to 4.5 THz with a high dynamic range exceeding even 100 dB at room temperature [42]. One can underline the desirable parameters for PCAs: high resistivity ($10^6 - 10^7$ Ω × cm) of the photoconductive material that allows reducing the dark current, yielding to a good signal-to-noise ratio (SNR) and preventing unnecessary heating of the device [44,45], high breakdown electric fields (∼ 500 kV/cm) [46], ultrashort photocarrier lifetimes (∼10–70 ps for pulse PCA-emitter and ∼ 0.5 ps for PCA-detector [47]) and sufficiently moderate photocarrier mobility (200–1000 cm^2/(V·s) [44, 46]. Note that pulse THz emitters, in general, do not require ultrashort photocarrier lifetimes as THz detectors [48], and can be successfully manufactured on ordinary single crystal structures [49]. The photoconductive THz photomixer that is utilized for CW THz generation comprises an ultrafast photoconductor integrated with a THz antenna. Nevertheless, its operation principle differs slightly and is as follows. When the photomixer is pumped with two optical beams with a beating frequency in the THz range, the photocarriers in photoconductor are drifted toward contact electrodes via applied bias voltage. The induced photocurrent is fed to the THz antenna to generate a CW THz radiation while the oscillation duty cycles would be comparable with the photocarrier lifetimes. Therefore, the photoconductive materials with very short photocarrier lifetimes and simultaneously moderate drift velocities are highly recommended for the photomixers [50–52].

Since Auston et al. demonstrated the ability to generate and detect the THz radiation using a silicon-on-sapphire photoconductive switch [53,54], the first material with significantly better performance has become a low-temperature grown GaAs (LT-GaAs) [55–58]. The appearance of the LT-GaAs has opened a new era in the development of the THz systems. Since that, the PCAs became among the mostly-used critical elements in the THz time-domain spectroscopic setups operating with 800 nm fs-lasers [17,18]. Basically, the LT-GaAs is a GaAs layer grown by molecular-beam epitaxy (MBE) on a GaAs wafer at the reduced growth temperature of 150 − 350 °C in an excess arsenic flow (whereas an ordinary growth temperature for GaAs with perfect crystal structure lies in the temperature range of 550–600 °C) that leads to the incorporation of non-stoichiometric arsenic atoms into the GaAs crystal lattice. The post-growth annealing at the temperature of 550 − 600 °C leads to the formation of arsenic precipitates. The lattice mismatch between the GaAs substrate and the LT-GaAs leads to a plastic relaxation of the crystalline lattice, especially for the epitaxial films grown below 200 °C. After reaching some growth-temperature-dependent critical thickness during the MBE growth, the LT-GaAs continues to grow in amorphous [59] or polycrystalline phases [60,61]. In the second case, the pyramidal defects with polycrystalline cores surrounded by the micro twins, stacking faults and other dislocations are usually formed [60]; however, the stacking faults are apparent in both cases. The authors in [61] demonstrated that strong depletion of As_{Ga} antisites can result in a longer photocarrier lifetime in the LT-GaAs featuring pyramidal defects or in the polycrystalline LT-GaAs. At the same time, the highest photoresponsivity was obtained in the layer with a density of pyramidal defects ∼10^7–10^8 cm^{-2} rather than in the perfectly or completely polycrystalline LT-GaAs. The sub-picosecond lifetime (∼0.4 ps), nevertheless, can be achieved in the polycrystalline LT-GaAs [62].

The alternative technique to reaching a short photocarrier lifetime, as well as high dark resistance, which is much simpler, cheaper and more reproducible compared to LT-growth, is the ion bombarding of semiconductors. In general, there are two techniques to generate traps and recombination centers in semiconductors for photocarriers, which

are ion implantation and ion irradiation. During ion implantation, the ions lose their energy through nuclear and electronic collisions and finally come to rest within the host material [19,20,63]. On the contrary, during ion irradiation, the ions have sufficient initial energy to leave the host crystal; hence, ion irradiation creates only intrinsic defects in semiconductors without introducing of impurities that result in residual absorption or modify dark resistivity of material [64]. The most important developments in the technology of THz PCAs fabricated on ion-bombarded semiconductors are reviewed in [65]. Moreover, the ion-bombarded GaAs shows some advantages over LT-GaAs. For example, N-implanted GaAs photomixers show no evidence of output power saturation that is typical for the LT-GaAs-based photomixers [19,20]. Also, the ion bombardment of semiconductors provides a spatial selectivity that can be useful for the manufacturing of different photonic devices on the same chip. Nevertheless, despite the ion concentration and the properties of the implanted material can be precisely and reproducibly controlled, the depth of the implantation is limited by at least several hundred nm. Also, ion bombardment does not provide the formation of sharp interfaces between thin layers of the multilayer structures.

We thus can conclude that to date, the research on optimal growth conditions has been already studied by many groups [43,66], and the further progress in the improvement of properties in bulk semiconductors is almost inaccessible. Therefore, many different multilayered designs of photoconductive structures have been proposed using various binary compounds and their combinations, notably AlAs heat spreading layers, DBR, InAs or ErAs QDs incorporated in photoconductive layers. Recently it was shown [67], that incorporation of an array of one-dimensional Sn-nanothreads channels situated along the edges of the vicinal GaAs terraces into GaAs matrix can be used as the sub-THz detector exhibiting the polarization sensitivity (i.e. selectivity) to the in-plane polarized THz wave. The detection principle is based on the two possible mechanisms, which are the bolometric mechanism due to electron heating by the sub-THz radiation and the subsequent evaporation of the electrons from the potential wells formed by the Sn-dopants and the mechanism related to the rectification of the decayed plasmonic oscillations. The fabricated detector exhibits the peak responsivity of 1.3 A/W at 0.13 THz at 300 K [68].

The simplest approach to increase the performance of the bulk photoconductive layer is to incorporate a wide bandgap isolation layer AlAs between the LT-GaAs and the semi-insulating GaAs wafer. The author of [69] demonstrated that this layer prevents the current diffusion into the substrate thanks to a higher energy bandgap and thus serves as an effective heat spreading layer. This approach was further implied in different structures for photomixers [70,71], photodetectors [72,73], pulse THz switches [74,75], etc. Since the AlAs layer is more often used in combination with design modifications as DBR or ErAs/GaAs SLs, it is inconveniently to estimate how this layer affects the PCA performance. However, the authors in [17] stated the improvement in the PCA's performance by using a 65 nm AlAs isolation layer. The layer was utilized to increase the arsenic incorporation in the LT-GaAs thanks to a larger lattice parameter compared to that for GaAs. Moreover, it provided a 23% optical back-reflection and enhanced the THz emission intensity. As a result, the LT-GaAs/AlAs-based PCA allowed obtaining a 4.5 THz bandwidth and a 75 dB SNR, whereas the same structure without the AlAs layer demonstrated 3 THz bandwidth with a 65 dB SNR.

Another efficient approach is related to the incorporation of a DBR. The DBR comprises a multi-period SL consisting of the layers with different refractive indexes located between the active photoconductive layer and the substrate. The SL is transparent to the THz pulse but reflects the unabsorbed part of the optical pulse to the photoconductive layer. This leads to an increase in an overall absorption of optical pump pulse and augments the quantum efficiency of the photoconductive structure. The DBR is mostly utilized as a standard technique to enhance the PCA's efficiency and is used in combination with various surface and structural modifications (for instance, with coating layers) to reduce optical transmission. The DBR implementation in a PCA's structure was first theoretically proposed in [76] to increase the output power of THz photomixer. The optimized LT-GaAs-based photomixer operating with a 0.85 μm optical pump included a 0.34 μm absorbing layer with a dielectric mirror to induce a resonant-cavity absorption near the surface where the gain is higher. The model has predicted ∼ 7 times greater THz output power compared to the photomixer without DBR. The first experimental study of DBR in THz emitter was demonstrated in [77], where the authors used 12-period AlAs/GaAs resonant cavity structures to enhance the LT-GaAs photomixer performance. The THz emitter demonstrated the output THz power of 1 μW at 460 GHz. Later in [78], the authors used a DBR consisted of 10–30 periods of $Al_{0.2}Ga_{0.8}As$/AlAs layers that were grown via MBE below the LT-GaAs layer. The THz emitter exhibited the 10-fold enhancement in the emitted THz power compared to the emitter without the DBR. Among a huge number of papers dedicated to DBR, we would underline several works. The authors of [75] proposed photoconductive switches based on either LT-GaAs or Be-doped InGaAs/InAlAs, which are both integrated with DBR to operate with 800 nm and 1550 nm optical pump, respectively. The introduction of DBR twice increased the THz peak signal as well as the photocurrent and doubled the optical-to-electrical efficiency. The authors in [79] proposed the THz detector based on a 280 nm thick LT-GaAs with an array of sparse optical nanoantennas on the top side of the layer and the GaAs/AlAs DBR at the bottom, which form a hybrid cavity to trap optical pulses within the LT-GaAs layer. The photon trapping effect was observed as an enhanced absorption at the designed wavelength, which led to an over 50% increase in the photocurrent. Later in [80], the LT-GaAs-based PCA with GaAs/AlAs DBR, recessed nanoplasmonic grating and recessed electrodes has been proposed. According to the author's simulation, the PCA resulted in a ∼ 54-fold photocurrent peak enhancement compared to the conventional LT-GaAs based PCA. Besides, in [26], it was experimentally demonstrated that the THz emitter including a nanocavity formed by the undoped high mobility 190 nm thick GaAs photoconductive layer with the plasmonic structure on its top, combined to a 25-period AlAs/$Al_{0.33}Ga_{0.67}As$ 60/55 nm thick DBR at the bottom, can generate 4 mW pulsed THz radiation under an average optical pump power of 720 mW over the 0.1–4 THz frequency range. It was claimed to be the highest ever-reported THz power obtained for the photoconductive THz emitters. Also, a DBR could be used in structures in a femtosecond laser cavity for highly efficient intracavity THz generation, where the photoconductive layer serves as a saturable absorber [81–83].

Theoretical predictions demonstrate that QDs [84,85] could also be used to increase the performance of the THz devices. Here we consider two main approaches that are based on ErAs and InAs QDs embedded into the GaAs matrix. The pioneering study of ErAs layers was reported by Sands et al. in [86]. The authors demonstrated that during the MBE growth, the first monolayer (ML) of ErAs is not growing uniformly and results in an island formation of ErAs with a height of 2 MLs. After 2 MLs of deposition, the regions between the islands fill in, and after 3 MLs a uniform layer can be seen (see Fig. 1). Such nucleation of ErAs in GaAs volume occurs in the island growth mode driven by the surface chemistry rather than by the strain (unlike the case of InAs self-assembled QDs). As a result, one can obtain the self-assembled 1 − 3 nm thick ErAs precipitates by choosing an appropriate concentration of Er-dopants [87]. The precipitates induce the mid-gap states at the ErAs/GaAs interface. These mid-gap states form very effective Shockley-Read-Hall recombination centers for photocarriers; their lifetime decreases correspondingly with an increase of the concentration of Er-dopants [33]. Besides, ErAs/GaAs layers demonstrate high resistivity, which is increased when the concentration of Er-dopants increases. Moreover, these layers can be grown at ordinary MBE temperatures resulting in a good crystalline quality of the layers as well as moderate photocarrier mobility compared to those for the LT-GaAs [88]. Thanks to a larger lattice parameter of ErAs (5.7427 Å) compared to GaAs

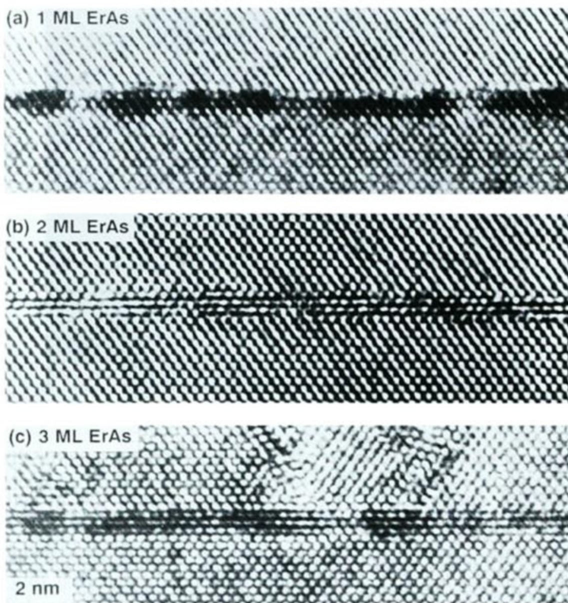

Fig. 1. High-resolution transmission electron microscopic (TEM) images illustrating GaAs/ErAs/GaAs structures with 1 (a), 2 (b) and 3 MLs (c) of ErAs. Adapted with permission from [86].

(5.6533 Å), ErAs/GaAs epitaxial films which are grown on GaAs wafer are weakly compressively strained. For instance, the residual strain is just 0.00042 even at a sufficiently high density of Er dopants ~ 5×10^{19} cm^{-3}.

By using the GaAs-based SL with ErAs islands (see Fig. 2a), one can control the photocarrier lifetime by changing the SL's period (see Fig. 2b). The authors of [23,33] demonstrated the shortest photocarrier lifetime of ~ 120E fs in a 20-period SL consisted of a 20 nm thick GaAs layer separated by a 1.2 ML of ErAs. At the same time, for the uniform ErAs precipitates distribution, the lifetime of photocarriers was ~ 1.5 ps. The density and the size of the ErAs islands can be adjusted by choosing the growth parameters: a higher growth temperature leads to a larger size of the ErAs islands, and a higher ErAs deposition results in a higher density of the ErAs islands. The subpicosecond response time of the ErAs/GaAs SL together with a high breakdown field exceeding 2×10^5 V/cm [89] makes the SLs perfectly suitable for THz photomixers. Although the photomixer in [23] based on the aforementioned structure demonstrated similar performance to the LT-GaAs-based THz devices, the maximum THz output power of the photomixer in [89] was registered of 0.1 μW at 1 THz. Bjarnason et al. in [71] reported on the fabrication and demonstration of ErAs:GaAs interdigitated photomixer − *a* tunable THz emitter operating from 20 GHz to 2 THz with a peak output power of 12 μW around 90 GHz. Also, in [90] the self-assembled ErAs:GaAs SL-based PCA was used to increase the THz detection. The authors compared 3 PCA-detectors. The first was fabricated on a 2 μm thick LT-GaAs, the second utilized a 500 μm thick radiation-damaged silicon-on-sapphire, and the third used the ErAs:GaAs SL. The SL comprised 80 periods each containing 1.2 MLs of ErAs nanoislands and 25 nm of GaAs. The last SL-based detector demonstrated a strong enhancement in the THz detection efficiency (291 times over the second and 157 times over the first one), but its performance degraded with the increase in optical power due to more rapid traps saturation of the ErAs:GaAs.

The properties of LuAs precipitates in GaAs, as well as its MBE growth parameters, are very similar to those for ErAs precipitates. Nevertheless, LuAs is more transparent in the near-infrared window around 1.3 μm [91]. The authors in [35] have investigated the impact of LuAs and ErAs nanoparticle depositions in ErAs/GaAs and LuAs/GaAs SLs, as well as the SLs period, on the THz emission using large-area plasmonic photoconductive pulsed THz emitters. Since the major portion of the generated THz emission from these emitters is due to ultrafast THz photocurrent fed to the nanoantenna arrays, the higher optical-to-THz conversion efficiency can be offered by layers with higher drift velocities of photocarriers. While ErAs/GaAs and LuAs/GaAs SLs with higher depositions of rare-earth arsenide (RE-As) degrade photocarrier drift velocities and, thus, the optical-to-THz conversion efficiency, the SLs with lower depositions of RE-As can increase both the drift velocity and optical-to-THz conversion compared to those for LT-GaAs. The abovementioned materials can also apply to plasmonic THz photomixers operating at a 780 nm laser wavelength as well [92]. It was shown that ErAs or LuAs nanoparticle deposition, as well as the SL's period, do not significantly affect the photocarrier lifetimes. Nevertheless, the ErAs/GaAs and LuAs/GaAs SLs with low ErAs and LuAs deposition respectively can offer a higher optical-to-THz conversion efficiency compared to the LT-GaAs, in particular in low-frequency region < 1 THz thanks to higher photocarrier drift velocity.

We can conclude that the parameters of the ErAs/GaAs SLs (resistivity, charge carrier mobility, and their lifetime) are competitive to those for the LT-GaAs. Thus, the ErAs/GaAs SLs have lost their attraction to excitation by 800 nm laser wavelength due to complexity in their fabrication compared to the LT-GaAs.

It is important to note that Er-doped bulk GaAs can be used with 1550 nm fiber laser thanks to the mechanism of extrinsic photoconductivity [93, 94]. When the concentration of Er-dopants exceeds 7×10^{17} cm^{-3}, they incorporate into the GaAs matrix and form ErAs QDs. The extrinsic photoconductivity process is excitation and ultrafast recombination of photoelectrons through mid-gap states associated with the ErAs QDs. Recently ErAs/GaAs-based PCAs in conjunction with a 1550 nm laser wavelength demonstrated ~ a 46 μW of the emitted THz power as well as the optical-to-THz conversion efficiency of 0.075% [29] and ~ a 117 μW of the emitted THz power with the

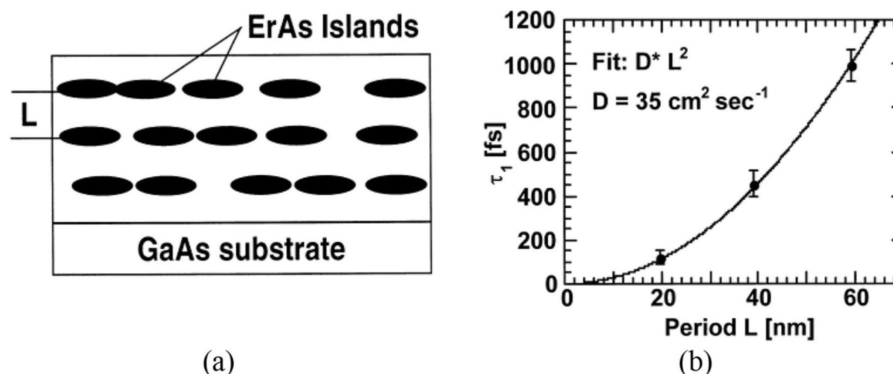

Fig. 2. Schematic cross-section of ErAs/GaAs QD-structure with SL (a) and a time constant τ_1 of the initial transient decay (photocarrier lifetime) as a function of the SL period L. Adapted with permission from [23].

0.18% efficiency [30]. High efficiency can be explained by Dicke superradiance, which the ErAs QDs demonstrate at room temperature due to cooperative spontaneous emission from the QDs optical dipoles [95].

Another approach is associated with InAs QDs formation on the GaAs surface. It is known that highly mismatched heteroepitaxy leads to the formation of self-assembled QDs [96,97]. Since that, the mechanisms of InAs QDs formation as a result of strain relaxation during the InAs/GaAs heteroepitaxy were studied thoroughly. The QDs formation is as follows. In the early stages of highly mismatched InAs on GaAs heteroepitaxy, self-assembled QDs appear in a strain-driven Stranski–Krastanov growth mode as soon as the coverage exceeds a critical value [98,99]. As was shown, the QDs appearance is determined by the preliminary growth of 2D platelets, which act as precursors for the formation of 3D coherent islands [100] exhibiting a small dispersion in size and shape. Moreover, it is possible to control the size and density of the QDs by choosing the respective growth conditions [101,102]. Up to date, some reviews have already been published and underlined the physics of InAs QDs formation [103] as well as their applications in mode-locked semiconductor lasers [104]. In this review, we will consider some of the recent results. We would mention that InAs QDs were used to significantly enhance the THz emission compared with the surface THz emission from bulk GaAs [105]. Moreover, they demonstrated a 70% of the emitted THz power compared to *p*-type InAs [24], which is the most intensive surface THz emitter. It was also concluded that multilayer InAs QDs consisted of 8 layers of InAs layers separated by 33 nm GaAs layers emit stronger THz radiation compared to single-layer InAs QDs (Fig. 3). The authors ascribe this phenomenon to huge strain fields at the InAs/GaAs interface. Since the QDs act as recombination centers for photocarriers generated in GaAs layers [106,107], the main advantages of using these structures can be applicable for PCAs. For instance, by using five 6 nm thick InAs QD layers separated by 10 nm GaAs spacers, it is possible to decrease photocarrier lifetime to ~ 1 ps [108]. The authors assume this is due to an increase in the capture area of the QDs at applied bias voltage. In addition, we note that first observation of CW-generation at 1.04 THz by using the THz photomixer comprising 40 periods of InAs QD layers separated by a 5 nm InGaAs wetting layer and a 35 nm GaAs layer, was demonstrated in [109].

The extensive study on InAs QDs structures was reported in [31]. The structures were grown via MBE in the Stranski–Krastanov growth mode and comprised a 30 nm top layer of LT-GaAs grown above active QD layer region of either 25 or 40 layers of InAs QDs immediately beneath. The QD layers were each capped by a 4–5 nm $In_{0.15}Ga_{0.85}As$ layer and separated by a 35–36 nm GaAs spacer layer, providing a total active region depth between 1 µm and 1.7 µm comprising either twenty-five or forty 40 nm QD sections. An extra spacer layer of GaAs was grown under the active photoconductive region (total thickness of the QDs) on an AlAs/GaAs DBR of either 25 or 30 layers. The QD structures were integrated with a dipole PCA. Measured wavelength dependencies of both QD THz emission obtained in the first experiment (blue curve on Fig. 4a) and the QD-based PCA-detector photoconductivity in the second experiment (red curve on Fig. 4a) show distinct peaks in the vicinity of the intra-dot electron transitions corresponding to the first and second excited state of the QDs. Hence, the QD-based PCAs can be used in conjunction with semiconductor laser pump sources operating in the 1.1–1.3 µm wavelength range. The apparent demonstration of QD-based PCA operating more efficiently when the more intensively it is pumped (Fig. 4b), can be explained by a higher photocarrier mobility and comparatively high thermal conductivity of the InAs:GaAs structures. Moreover, the increased efficiency could also be coupled with the effect of photocarrier lifetime shortening in QDs with an increase of optical pump power, similar to that exhibited in QD-based semiconductor saturable absorber mirror [106]. This phenomenon was studied in detail in the recent paper [110], where the authors ascertained that photocarrier lifetime shortening in similar to the abovementioned QDs structures design but for higher pump powers in the unbiased PCA is due to increased photocarrier capture via Auger relaxation.

The authors of [32] have demonstrated the generation of a tunable THz signal from a room-temperature all-semiconductor InAs/GaAs QD based setup, involving a QD based photomixer resonantly pumped by a broadly-tunable dual-wavelength QD laser. The active region of the laser chip contained 10 non-identical layers of InAs QDs grown on a GaAs wafer by MBE in the Stranski-Krastanov growth mode. The PCA's structure comprised 40 layers of InAs QDs, each capped by a 4-nm $In_{0.15}Ga_{0.85}As$ and separated by 36-nm GaAs spacer layers, giving a total of 1 µm depth active region. The CW THz generation was observed at 0.83 THz and 0.74 THz with a maximum output power of 0.6 nW at 0.83 THz with the pump QD laser operating in the dual-wavelength regime (1161.1 nm and 1157.4 nm with 89 mW and 83 mW optical power, accordingly).

1.1.2. Ternary and quaternary compounds

The expansion of fiber lasers has developed a strong interest in narrow-bandgap semiconductor-based materials that can efficiently operate with longwave optical pumps of 1.03 − 1.55 µm emitted by fiber lasers and neodymium glass lasers allowing for fabricating of the cost-effective and compact THz emitters/detectors for THz spectroscopic and imaging systems. The most commonly used photoconductor has become $In_{0.53}Ga_{0.47}As$ that has the energy bandgap of E_g = 0.74 eV (at 300 K) compared to E_g = 1.508 eV at 300 K for the LT-GaAs [111–113] and that can be used for both pulse and CW THz generation [112,114]. Note that varying the indium content (x) in $In_xGa_{1-x}As$, one can adjust its energy bandgap to the wavelength of the fs-laser

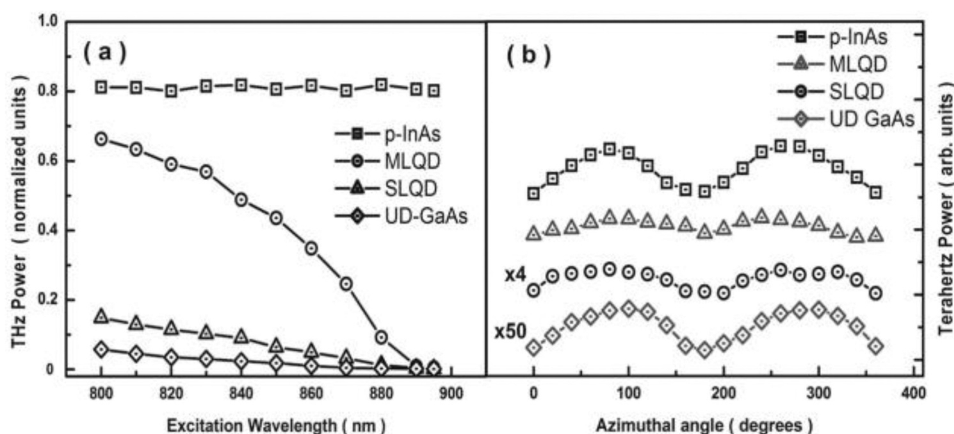

Fig. 3. The excitation wavelength spectra comparison for the multilayered (ML) and single-layered (SL) InAs QD structures, *p*-InAs, and undoped (UD) GaAs (a) and azimuthal angle dependence on the emitted THz power (b). Adapted with permission from [24].

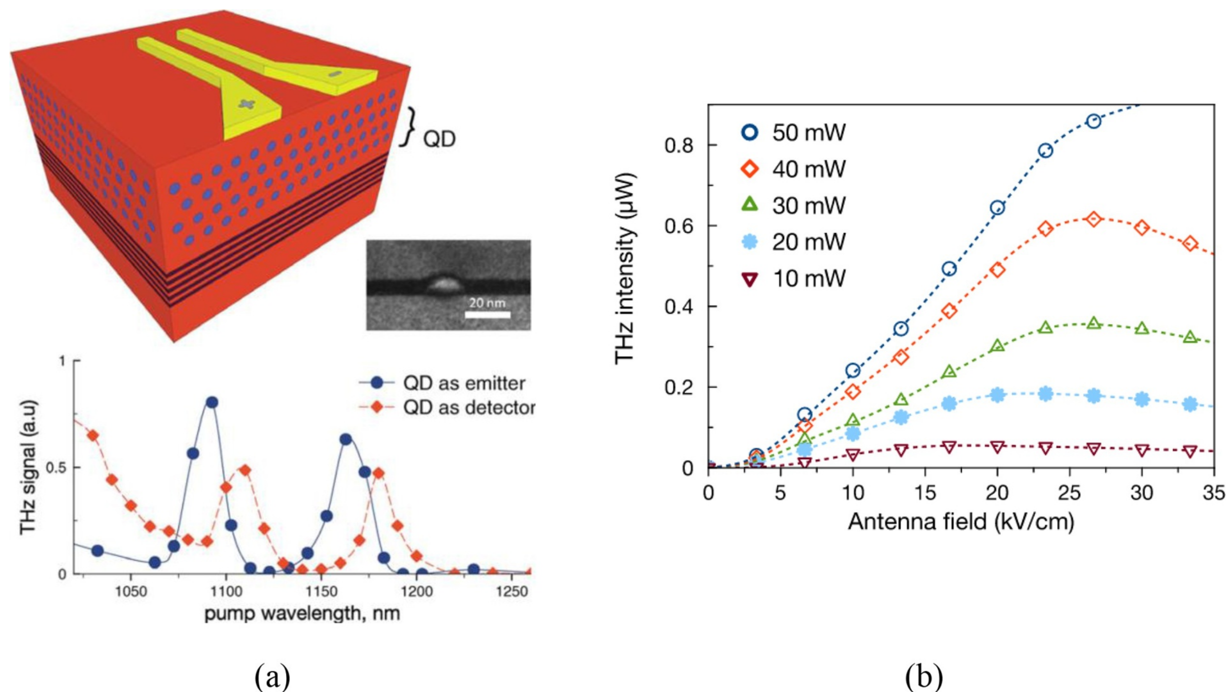

Fig. 4. (a) Registered by GaBiAs detector (blue) and emitted by InAs crystal surface and registered by QD detector (red) pump wavelength dependencies of THz signals, GS – ground state, ES1 – first excited state, ES2 – second excited state. On the inset TEM image of a single QD. (b) THz power at different fields applied to antenna from a 25 layer QD PCA pumped using 800 nm laser. Adapted with permission from [31]. (For interpretation of the references to colour in this figure legend, the reader is referred to the web version of this article.)

excitation [114–116]. Besides, we notice that via a metamorphic buffer (MB) one can vary the indium content in a wide range of 0 − 100% regardless of the type of the wafer (GaAs or InP) [115–117].

Basically, due to large difference in the diffusion coefficients of electrons and holes, a bulk InGaAs can emit THz radiation as a result of the boundary conditions on the carrier transport within a semiconductor due to the surface-field acceleration [118] and the photo-Dember (PD) effect [119]. Since the THz power emitted by the PD-emitters is quite low, the lateral PD-emitters (LPD) have been proposed to increase the THz radiation efficiency [120,121]; it was shown that an array of the LPDs could significantly increase the emitted THz power, nevertheless still unable to compete with the biased PCAs [122,123].

The important fact is that thanks to high photocarrier relaxation time combined with low resistivity of the photoconductive material, it is impossible to fabricate the efficient PCA-emitter based on the bulk InGaAs owing to high dark currents, which are detrimental for the PCA's performance. Accordingly, various approaches have been proposed to reduce photocarrier relaxation times of InGaAs, and most of them are associated with multilayer designs and thus will be described below. The others include different modifications of bulk InGaAs, for instance Be-doped LT-InGaAs [124,125], Fe-doped InGaAs [126,127] as well as heavy ion-implated [128,129] or ion-irradiated defects in InGaAs [130,131]. Recently, THz emission has been reported for InGaAs nanowire arrays [132].

The pioneering works were dedicated to the heterostructure SLs grown via MBE and consisted of Be-doped LT-InGaAs photoconductive layers sandwiched between InAlAs barrier layers [133–135]. Note that this design became the most effective approach to increase the resistivity of LT-InGaAs thanks to the proximity of As_{Ga} related energy levels to the conduction band, which leads to high residual concentration of charge carriers [125,136]. The LT-InGaAs/InAlAs SLs demonstrate advantages above the bulk LT-InGaAs since the LT-InAlAs layers can provide deep trap states that are situated energetically below the As_{Ga} levels of the adjacent InGaAs layer [137]. In contrast, very short photocarrier lifetimes allow fabricating efficient THz detectors or photomixers operating at the telecom wavelength. The lattice-matched Be-doped LT-InGaAs/InAlAs SLs can exhibit sub-picosecond lifetimes (< 200 fs) and the resistivity $\sim 10^7$ Ω/sq at the optimized combination of doping and annealing temperature [138]. Using the Be-doped $In_{0.53}Ga_{0.47}As/In_{0.52}Al_{0.48}As$ SL with a total thickness of 1 μm and a photocarrier lifetime ~ 0.2 ps, the authors of [139] fabricated a THz detector featuring a 90 dB dynamic range and a 6 THz frequency bandwidth. Recently the record high dynamic ranges of 70 dB at 3 THz and 55 dB at 4 THz, respectively have been demonstrated on the PCA-detectors based on the InGaAs/InAlAs SLs with a localized Be-doping of the InAlAs barrier layers allowing intensification of the electron trapping [140]. These structures could be also used for THz photomixing at the telecom wavelengths [141,142],.

Dietz et al. [34] proposed the $In_{0.53}Ga_{0.47}As/In_{0.52}Al_{0.48}As$ SL, which is lattice-matched to InP wafer. The SL utilized the undoped high-mobility $In_{0.53}Ga_{0.47}As$ layers without the implementation of As_{Ga} defects. The electron mobility in such structures can reach $1500 - 3000$ cm^2/(V·s). The layout of the InGaAs/InAlAs SL and the band diagram illustrating its operation principle are depicted in Fig. 5. The authors investigated the MBE growth of the InAlAs barriers and settled up that formation of InAs and AlAs clusters is responsible for alloy scattering of the photocarriers at the reduced growth temperature of $300 - 500$ °C. The latter means the appearance of deep electron traps states in the middle of the InAlAs energy bandgap [137], which is crucial for the recombination of the excess photocarriers. Note that TEM image of the SL grown at 400 °C via MBE illustrating clusters segregation will be shown below in Fig. 7. The SL-based PCA has demonstrated the increase in optical-to-THz conversion efficiency up to one order of the magnitude, featuring a 3 THz frequency bandwidth.

During the further studies of these structures in [27], the authors determined the optimal growth temperature range of $350 - 375$ °C, which is essential to reduce the photocarrier lifetime. However, the THz emission intensity is decreasing with an increase of trap state density, and the optimal growth temperature concerning the maximum THz emission was fixed at 400 °C. Nevertheless, the 100-period

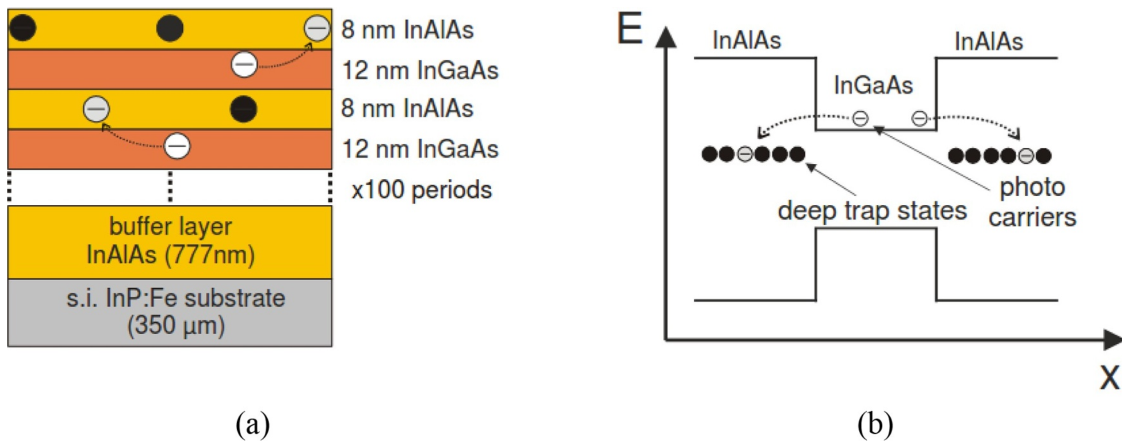

Fig. 5. The layout of 100 periods undoped $In_{0.53}Ga_{0.47}As/In_{0.52}Al_{0.48}As$ SL with cluster-induced defects acting as electron traps (indicated by black circles) (a) and the band-diagram in a real space with deep cluster-induced defect states illustrating an operation principle of the SL (b). Reprinted with permission from Roman J. B. Dietz, Marina Gerhard, Dennis Stanze, Martin Koch, Bernd Sartorius, and Martin Schell, "THz generation at 1.55 µm excitation: six-fold increase in THz conversion efficiency by separated photoconductive and trapping regions," Opt. Express 19, 25911-25917 (2011) © The Optical Society. [34].

$In_{0.53}Ga_{0.47}As/In_{0.52}Al_{0.48}As$ (12/2 nm) SL grown at the optimized growth temperature demonstrated a 64 µW of the emitted THz power at a 32 mW of optical excitation. In other words, these results correspond to the optical-to-THz conversion efficiency of 2×10^{-3}, which is two orders of the magnitude higher compared to that for the LT-Be-doped InGaAs/InAlAs SL.

It is also important to note that special attention should be paid to a proper choice of InAlAs barrier thickness, as it was shown in [143]. The author has derived the probability densities for two electron wave functions (WFs) in the first subband by solving the 1D Schrödinger equation in a 30-period $In_{0.53}Ga_{0.47}As/In_{0.52}Al_{0.48}As$ SL. The band diagrams of a pair of SLs with the same 12 nm thick $In_{0.53}Ga_{0.47}As$ photoconductive layer sandwiched between the $In_{0.52}Al_{0.48}As$ barrier layers with the thicknesses of 16 and 2 nm were compared (see Fig. 6). It was demonstrated that when using relatively thin barriers, the electron WFs will strongly overlap with the trap states in the barriers compared to the case with the thick barriers; this is since the fact that the penetration depth of the electron WF is limited by the conduction band offset between the $In_{0.52}Al_{0.48}As$ and $In_{0.53}Ga_{0.47}As$ layers, i.e. the barrier height. Hence, the defect states situated deep inside the barriers are not available for the electrons in the InGaAs photoconductive

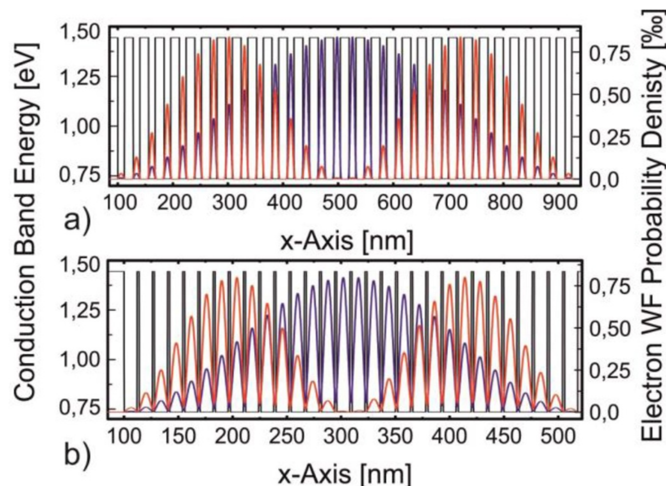

Fig. 6. Two electron wave functions of the first subband together with the conduction band energies calculated for the lattice-matched $In_{0.53}Ga_{0.47}As/In_{0.52}Al_{0.48}As$ SL with a 12 nm thick $In_{0.53}Ga_{0.47}As$ photoconductive layer and $In_{0.52}Al_{0.48}As$ barrier layer with the thicknesses of 16 nm (a) and 2 nm (b). Adapted with permission from [143].

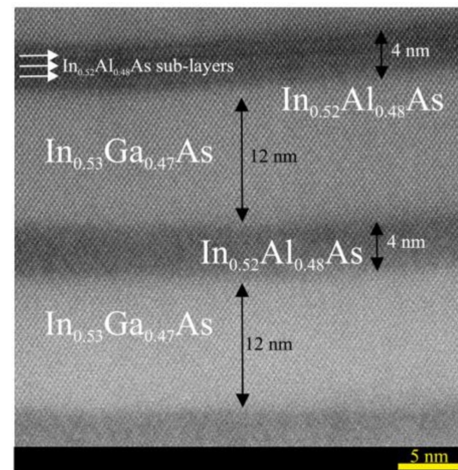

Fig. 7. Dark-field TEM-image of the nonstrained $In_{0.53}Ga_{0.47}As/In_{0.52}Al_{0.48}As$ SL with layers thicknesses of 12 nm and 4 nm, respectively. The $In_{0.52}Al_{0.48}As$ sublayers, approximately of 1–2 nm thick, referred to defect levels formation, are seen in the $In_{0.52}Al_{0.48}As$ barrier layers (indicated by horizontal arrows). Courtesy by A.E. Yachmenev and D.S. Ponomarev.

layers.

The recent progress in high mobility multilayered heterostructures has been demonstrated in [28], where the authors proposed a 30-period LT-InGaAs/InAlAs strain-induced SL. The SL utilized the step-graded MB consisted of 5 InAlAs layers of a 0.15 µm thickness each with the increase in the indium mole fraction by 10% in each consequent layer. The artificial decrease of the indium content in the barrier layers up to $In_{0.38}Al_{0.62}As$ (compared to $In_{0.52}Al_{0.48}As$) lead to the residual strain in the SL. The strained SL demonstrated a 3-fold reduction in the photocarrier lifetime compared to those for the lattice-matched SL thanks to the additional scattering mechanisms caused by the residual strain (the interface roughness and the micro alloy scattering) [28, 144,145]. Also, the authors demonstrated a 10-fold increase in the emitted THz power in the strained SL, since the residual strain provides a decrease in the energy bandgap of the $In_{0.53}Ga_{0.47}As$ photoconductive layer which as a consequence, increases the photon excess energy of the photocarriers.

Similar to GaAs, the doping by Er atoms can be successfully implemented to InGaAs to reduce the photocarrier lifetime. Nevertheless, one should underline the critical difference between the ErAs/GaAs and the ErAs/InGaAs structures. In the first case, the Er-doping results in both high resistivity and sub-picosecond photocarrier lifetime in GaAs,

while in the case of the ErAs/InGaAs, the photocarriers have a longer lifetime. At the same time, the InGaAs demonstrates reduced dark resistivity and a relatively low breakdown voltage. These are mostly since the incorporation of Er atoms into the InGaAs shifts the Fermi level close to or above the conduction band edge, and the ErAs/InGaAs evinces *n*-type conductivity [146]. It should be noted that the dark resistivity can be increased by compensating conductivity of the electrons in the ErAs/InGaAs by *p*-type dopants, and thus the Fermi level can be tuned toward midgap [147,148]. In [149], the authors have studied SLs consisted of layers of semi-metallic ErAs nanoparticles embedded into $In_{0.53}Ga_{0.47}As$ matrix, which were grown by MBE on (100) semi-insulating InP wafers at a temperature of 490 °C. The time-resolved optical measurements revealed that the photocarrier lifetime decreases with both an increase in ErAs deposition and Be compensation doping as well as the decrease of SL's period. The shortest photocarrier lifetime was 0.3 ps in a sample with 0.8 ML of ErAs, 5 nm period, and a Be delta-doping concentration of 5×10^{13} cm^{-2}, with thus demonstrating superior properties for PCA applications. As was shown in [25], the photocarrier lifetime can be tuned from 0.22 to 6.3 ps by changing the periodicity of ErAs:InGaAs SL from 5 to 100 nm, respectively. Later Schwagmann et al. characterized ErAs:$In_{0.53}Ga_{0.47}As$ SLs as photoconductive THz emitters excited at 1.55 μm wavelength [150]. The ErAs:$In_{0.53}Ga_{0.47}As$ SLs were grown by MBE at 490 °C using a semi-insulating (100) InP wafers with a 250 nm thick $In_{0.52}Al_{0.48}As$ buffer layer. The SL was fabricated by alternatingly growing layers of the self-assembled ErAs islands and $In_{0.53}Ga_{0.47}As$ spacers with the SL period (L). Two sets of SLs were used: structures with L ranging between 5 and 20 nm comprise the SL with a total thickness of 500 nm, an amount of ErAs per island layer equivalent to 0.8 ML and Be δ-doping with a density of 5×10^{13} cm^{-2} in the immediate vicinity of this layer to compensate free electron concentration. Structures with L ranging from 30 to 100 nm have a 1200 nm thick SL and 1.75 ML ErAs deposition per SL period. A region extending 2.5 nm above and below the island plane is uniformly doped with a local Be concentration of 1×10^{20} cm^{-3}. The structures then were combined to a bow-tie PCA. The definitions of the investigated parameters are shown in Fig. 8a. As seen in Fig. 8b, a variation in the electron lifetime from 0.2 to 6.3 ps (owing to L varying) does not considerably influence the THz bandwidth (Δf) of the emitted radiation, and the Δf does increase with increasing bias field (see Fig. 8c).

In [151] Preu et al. reported on a high power THz emission from ErAs-enhanced $In_{0.52}Al_{0.48}As/In_{0.53}Ga_{0.47}As$ SLs operating at 1550 nm. The photoconductive layer consisted of a 70-period SL comprising a 15 nm $In_{0.53}Ga_{0.47}As$ layer, a 2.5 nm $In_{0.52}Al_{0.48}As$ layer, 0.8 monolayers of ErAs, and a 2.5 nm $In_{0.52}Al_{0.48}As$ layer. The ErAs layer was Be-doped with an acceptor concentration of 5×10^{13} cm^{-2}. A THz field strength of 0.7 V/cm at 100 mW average optical power, as well as emission up to about 4 THz were obtained.

Another high-power and broadband photoconductive THz emitter utilizing a very short photocarrier lifetime in ErAs:InGaAs photoconductive layer was demonstrated in [152]. The emitting device consisted of 1 μm thick ErAs:InGaAs layer with a photocarrier lifetime of 1.24 ps, which was grown via MBE on semi-insulating InP wafer, and employed a two-dimensional array of plasmonic nano-antennas. The authors showed radiation powers as high as 300 μW over 0.1–5 THz frequency range that is the highest ever-reported THz radiation power from the photoconductive THz emitters operating at telecommunication wavelength.

Later Olvera et al. demonstrated CW generation and detection of the THz waves using a photomixer based on ErAs:In(Al)GaAs SL [153]. The SL-based detector comprised an intrinsic 10 nm thick InGaAs layer and 0.8 ML of a δ-*p*-doped semi-metallic ErAs. The band diagram of the SL is illustrated in Fig. 9a. The SL was grown at the optimized growth temperature around 490 °C for the InGaAs layer. A THz photoconductive emitter had a slightly different design. In addition to the intrinsic InGaAs layer and *p*-doped ErAs, the authors included a 2.5 nm InAlAs layer in the SL's structure to increase the breakdown field strength.

The schematic band diagrams of 1.5 period are illustrated in Fig. 9b. The emitter demonstrated a breakdown field of 170 kV/cm. The samples were δ-doped with a concentration of 10^{13} cm^{-2}. The log-spiral PCAs were fabricated on top of the SLs while the average pump power of each fiber laser was 26 mW. To the knowledge of the authors, the measured dynamic range 52 dB (31.7 dB) at 1 THz (2 THz) is the highest dynamic range ever reported for a CW system operating at 1550 nm and using only photoconductive elements. Also, the extrapolated bandwidth of 3.65 THz within peak dynamic range of 78 dB is on the level of the largest bandwidths, which have been reported to date with any 1550 nm CW THz system (see Fig. 10).

Alike for RE GaAs-based SLs, not only Er nanoislands can be used to improve the InGaAs parameters. The InGaAs-based SLs involving

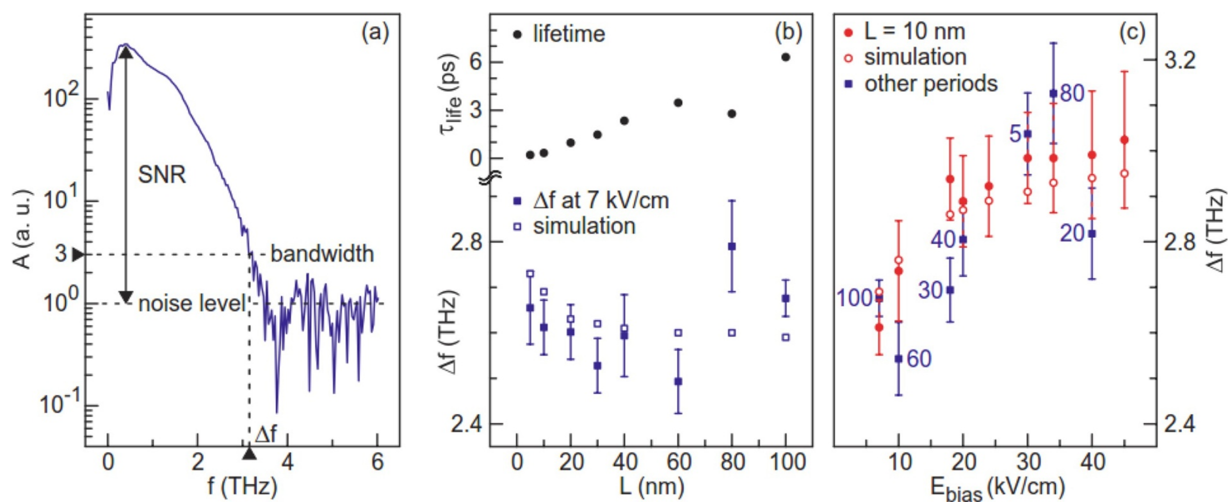

Fig. 8. Typical spectrum of a THz pulse form with SNR and bandwidth definitions (a); electron lifetimes (black disks) and experimental (blue solid squares) and simulated (blue open squares) bandwidths for 7 kV/cm bias field as a function of the SL period L (b); the THz bandwidths as a function of applied bias field (c). The blue solid squares represent bandwidths for PCAs operating at their maximum safe bias field. The numbers next to the data points indicate the SL periods L. The red disks display bandwidths for the reference SL with $L = 10$ nm, the red open circles give the corresponding simulated values. Reprinted with permission from A.D.J. Fernandez Olvera, H. Lu, A. C. Gossard, and S. Preu, "Continuous-wave 1550 nm operated terahertz system using ErAs:In(Al)GaAs photo-conductors with 52 dB dynamic range at 1 THz," Opt. Express 25, 29492-29500 (2017) © The Optical Society [150]. (For interpretation of the references to colour in this figure legend, the reader is referred to the web version of this article.)

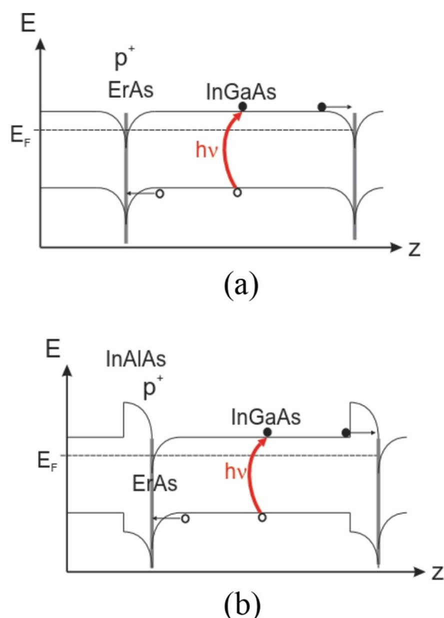

Fig. 9. The schematic band diagrams of 1.5 period of (a) detector and (b) emitter. Adapted with permission from [153].

compositions of LuAs, GdAs, and LaAs have been proposed and studied [154]. Nevertheless, these compounds expose diversity in the electrical properties of the InGaAs. For instance, LaAs:InGaAs was found to have the highest dark resistivity of 0.18 Ω × cm together with the lowest electron mobility 1600 cm^2/V s and photocarrier lifetime of 5.4 ps. The GdAs:InGaAs demonstrated the shortest photocarrier lifetimes 1.7 ps and the highest electron mobility 2400 cm^2/V s. The SLs comprising the LuAs nanoparticles embedded into $In_{0.53}Ga_{0.47}As$ layers were studied in detail in [155,156]. The SL structure consisted of a 150 nm InGaAs buffer layer followed by 30 periods of InGaAs/LuAs grown at 490 °C. A combination of the bismuth surfactant usage during the InGaAs growth and lower LuAs growth rates of 0.01 ML/s (2.8 ML LuAs deposition) have enabled a significant reduction in photocarrier lifetime to 1.6 ps despite the large SL's period of 40 nm. However, all these materials are rather exotic to be used for conventional PCAs.

Quaternary compounds can also be used for THz photoconductive emitters although much less common compared to binary or ternary compounds. For instance, in [157,158], the authors used a Fe-implanted InGaAsP layer which exhibited resistivity of 2.5 kΩ × cm and Hall mobility around 400 cm^2/V × s. Later in [159] it was suggested to use a Fe-doping of InGaAsP instead of ion implantation. Thanks to better control over the Fe compensator distribution, the doping produces less damage to the crystalline structure. The authors used a 1 µm thick Fe:$In_{0.7}Ga_{0.3}As_{0.87}P_{0.13}$ photoconductive layer with E_g = 0.8 eV and InP buffer/cap layers. Compared to the Fe-doped $In_{0.53}Ga_{0.47}As$, one has discovered the enhanced surface homogeneity and the increased resistivity of the layer up to 10 kΩ × cm, while the measured THz power was about ~50 µW. In [160], the authors proposed bulk quaternary alloy of GaInAsBi epitaxial layers with 6% Bi that was grown by MBE on InP wafer. It has been found that 0.6 µm thick GaInAsBi layers remain strained due to the relatively small lattice mismatch with InP wafer compared to the similar layers grown on GaAs wafer, which become entirely relaxed [161]. The authors demonstrated the photocarrier lifetime of 3–4 ps and the resistivity of 5 Ω × cm. Thanks to their relatively small energy bandgap E_g = 0.4 eV, these photoconductive structures seem to be promising due to the possibility of using optical pump pulses with wavelengths longer than 2 µm.

The comparison between material properties and PCA parameters for different binary and compound multilayered semiconductors is summarized in Table 1.

1.2. Structures with p-i-n design

In this section, we consider multilayer structures used for *p-i-n* diodes to generate a pulse and CW THz radiation. The *p-i-n* diodes have become among the promising devices for the THz photomixers that can efficiently operate at room temperature.

At the beginning of the 90 s, the demonstration of the THz emission using the *p-i-n* diodes based on silicon was reported in [162]. The authors showed that in contrary to the PCA's photoconductive layer, the *p-i-n* diode should provide a perfect crystalline structure of the intrinsic layer, without any defects and impurities, allowing for ballistic electron transport. In addition, the one more difference from the PCA lies in the photocurrent of the *p-i-n* diode that is defined by vertical transport of the photocarriers under built-in or external electric fields. Moreover, the large-aperture *p-i-n* diodes can potentially demonstrate the stronger THz emission at high optical fluences.

The first THz emission in the GaAs-based *p-i-n* structure under fs-pulse excitation was registered in [163]. The structure comprised a highly *n*-doped GaAs layer, a 1 µm thick n^+-GaAs buffer layer, a 0.3 µm thick intrinsic GaAs layer, and a 20 nm p^+-GaAs. It was found that the THz emission can be enhanced compared to a similar structure on silicon.

Later, the theoretical and experimental study of the non-biased GaAs structures revealed that the THz emission in the *p-i-n* structures appears due to the incoherent plasma oscillations of the photocarriers caused by oscillations of the built-in electric field. Such plasma oscillations lie in the THz frequency range [164–166],. However, the practical use of these structures is limited due to the low power of the emitted THz waves. In [167], A. Reklaitis has theoretically demonstrated that a low efficiency is due to the incoherent plasma excitations

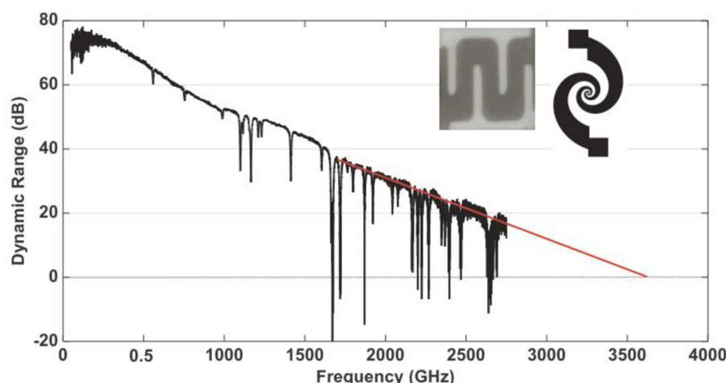

Fig. 10. The dynamic range of a CW THz spectroscopic system using only ErAs:In(Al)GaAs photoconductors. The insets show the used the electrode structure and the spiral PCA. Adapted with permission from [153].

Table 1
Comparison between material properties and PCA parameters for different binary and compound multilayered semiconductors.

Material	Material properties			PCA performance					Refs.
	Resistivity, $\Omega \times cm$	Mobility, $cm^2/(V \times s)$	Photocarrier lifetime, ps	Pulsed (P) or continuous-wave (CW) operation regime	Excitation wavelength, nm	Dynamic range, dB	Bandwidth, THz (P regime)or generation frequency, THz (CW regime)	THz power,μW	
LT-GaAs	10^7	164	0.2	P	780	80	7	–	[47,58]
	–	–	0.25	CW	800	–	1	2	[52]
Ion-implanted GaAs	5×10^4	150	~ 0.3	P	780	–	2.5	–	[63,65]
	–	–	0.11	CW	780	–	1	0.13	[19]
Ion-irradiated GaAs	–	–	0.2	CW	800	–	0.1	0.06	[64]
ErAs/GaAs	–	> 100	0.67	P	800	70	4	1400*	[35,71]
QDs SL	2.4×10^4	–	0.12	CW	850	–	1	0.1	[89]
LuAs/GaAs	–	–	0.65	P	800	70	4.5	1200*	[35]
QDs SL	10^4	–	0.65	CW	780	–	< 1	–	[92]
InAs/GaAs	–	1000	3–6	P	810	20	2	0.83	[31,110]
QDs SL	–	–	–	CW	1160	–	0.83	6×10^{-4}	[32]
Ion-irradiated InGaAs	3	490	0.2	P	1550	30	3	–	[130]
Ion-implanted InGaAs	6.1×10^3**	1500	–	P	1560	25	2.5	–	[128,129]
Fe-doped InGaAs	2×10^3	900	0.3	P	1560	50	6	75	[127]
Be-doped LT-InGaAs	0.7×10^3	100 – 1000	–	P	1560	55	3	–	[124]
Be-doped LT-InGaAs/	$\sim 10^7$**	500 – 1800	< 0.2	P	1550	90	> 6	–	[138,139]
InAlAs SL	–	–	–	CW	1550	–	1	0.4	[142]
Lattice matched InGaAs/ InAlAs SL	5.8×10^3	1500 – 3000	12.8	P	1550	30	> 4	64	[27,34]
Strained InGaAs/InAlAs SL	$\sim 9 \times 10^3$	1600	~ 1.7	P	800	< 20***	3***	–	[28]
Be-doped ErAs/InGaAs	$< 3.4 \times 10^2$	1380	2.2	P	1550	51	4	–	[25,151]
QDs SL	–	–	1.3	CW	1550	52	1	–	[153]

* large-area THz emitter.
** sheet resistance.
*** surface THz emitter.

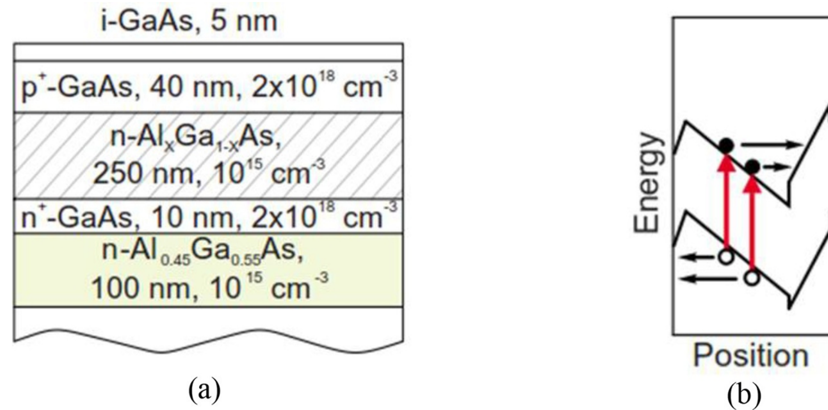

Fig. 11. Design of one period of the structure (a) and illustration of band profile and photocarrier dynamics in the structure immediately after the photoexcitation (b). Adapted with permission from [168].

that reduce the intensity of the THz emission. He suggested using the δ-doped multiperiodic AlGaAs/GaAs heterostructure for the coherent plasma excitations. Using the Monte Carlo simulations, he demonstrated that the efficiency of the THz emission exceeds the efficiency of the surface THz emission and from the bulk *p-i-n* structure by 2 orders of magnitude.

The experimental study of the proposed heterostructure was realized in [168]. The design of the heterostructure implied 5 periods of the 100 nm undoped $Al_xGa_{1-x}As/Al_{0.45}Ga_{0.55}As$ layers. Alternating *n*- and *p*-type δ-doped GaAs layers were inserted at the $Al_xGa_{1-x}As/Al_{0.45}Ga_{0.55}As$ interfaces; the thickness of these layers amounts to a 10 nm each with the exception for the first p^+-GaAs layer which had a thickness of 40 nm. The different Al mole fractions in the $Al_xGa_{1-x}As$ layers ranging from $x = 0.08$ on top in the first period to $x = 0$ in the fifth period at its bottom were selected to ensure an equal average electron and hole densities in each layer upon the photoexcitation. The design of the one period of the considered structure and the schematics of the photocarrier dynamics are depicted in Fig. 11. As a result, it was shown that the emitted THz power from the δ-doped GaAs/AlGaAs *p-i-n* heterostructure surface emitter is competitive with that from the InGaAs and *p*-InAs surface THz emitters.

Thanks to their relatively high efficiency and elevated THz power, the *p-i-n* diodes featuring specific designs which will be discussed below, have become among the promising devices for the THz photomixing, in particular operating at the telecom wavelength. The THz photomixing allows generating a CW THz radiation when two optical pulses with a beating frequency in the THz frequency range are mixed and incident on the photomixer [112].

In the pioneering work [169], the authors have designed and fabricated a 0.460 THz photomixer (optical-to-electrical power converter). The InP-based waveguide structure of the *p-i-n* detector consisted of the *p*-doped InAlAs cladding layer on the top, a 100 nm InGaAs absorbing layer, InGaAsP passive core layer, and *n*-doped InP cladding layer at the bottom.

One of the first approaches aimed at the improvement of the emitted THz power compared to the conventional *p-i-n* structure implied a uni-traveling-carrier photodiode (UTC-PD). The operation principle of the UTC-PD is as follows: when the optical pulse falls, the photoelectrons in the neutral absorption layer diffuse into the depleted collection layer. Thanks to the quasi-neutrality of the absorption layer, the photo-generated holes respond very fast within the dielectric relaxation time by their collective motion. Therefore, the photoresponse of the UTC-PD is determined only by the electron transport in the whole structure that severely differs from that for the conventional *p-i-n*-PD where both electrons and holes contribute to the response current, and low-velocity hole-transport predominantly determines the performance of the device.

The authors in [170] proposed the design of the UTC-PD which active area consists of a 90 nm thick *p*-type narrow bandgap absorption layer comprising a *p*-InGaAs layer, a thin p^+-InGaAs, and an undoped InGaAs layers and a 282 nm thick undoped (or slightly *n*-doped) wide bandgap depleted carrier-collection layer comprising a thin undoped InGaAsP layer, a thin undoped InP and n^+-InP layers and slightly *n*-doped or undoped InP layer. Thin InGaAsP layer provides a step-graded bandgap profile and is required to suppress current blocking at the absorption/collection layer interface. The heterostructure was grown on a (100)-oriented semi-insulating InP wafer via a low-pressure MOCVD using C and Si as donor and acceptor dopants, respectively. The fabricated device exhibited an output power of 300 μW and 2.6 μW at 0.3 THz and 1.04 THz, respectively, depending on a type of the coupled antenna. Later in [171], the authors demonstrated the output power of several mW by using the UTC-PD in the sub-THz range up to 300 THz. The layout of the UTC-PD is depicted in Fig. 12.

Another concept for the THz photomixers is based on a ballistic transport of the photoelectrons in a stack of nanoscale *p-i-n* diodes instead of a single *p-i-n*-diode. The first theoretical analysis of this approach was carried out in [172], while the experimental confirmation of the ballistic transport in the *n-i-p-n-i-p* SL-based photomixer was demonstrated by S. Preu et al. in [173]. The basic idea is to use the SL stacks consisting of several *p-i-n* diodes instead of the single *p-i-n* diode. Each *p-i-n* diode is optimized to minimize the carrier transit time that can be achieved by a sufficiently short intrinsic layer allowing for

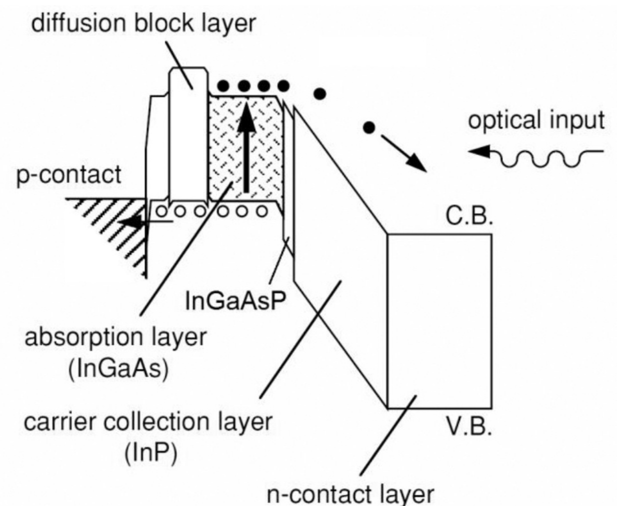

Fig. 12. Band diagram illustrating operation principle of the UTC-PD. Adapted with permission from [170].

ballistic transport and thus has no significant transit-time roll-off at the desired THz frequency [172,112]. The authors demonstrated the emitted THz power of 1 μW at 0.4 THz in the CW regime using the two-period InGaAs photomixer with the incorporated log-periodic PCA.

Alternatively to the CW generation, the authors in [174] studied the *n-i-p-n-i-p* SL-based structure in the pulse THz regime. The design of the SL comprised a 3-period *n-i-p-n-i-p* SL photomixer with an intrinsic layer consisted of a 150 nm long linear Al-grading from $In_{0.53}Ga_{0.47}As$ to $In_{0.53}Al_{0.08}Ga_{0.39}As$ towards the *n*-contact, followed by a 50 nm $In_{0.53}Al_{0.08}Ga_{0.39}As$ transport layer. The majority of the carriers are generated in the first 50 nm of the graded layer. At the interface of the diodes, a quasi-metallic ErAs-layer is implemented in order to provide direct tunneling of electrons and holes into the ErAs layer and thus increase the recombination current [112]. The authors demonstrated that the *n-i-p-n-i-p* SL photomixers are efficient THz emitters for both CW and pulse operation and comparable to a large-area InGaAs-based photoconductive THz emitters operating with the telecom wavelength [175].

2. Multilayered structures for THz QCL

In this section, we consider the technique of the MBE growth and optimization of multilayered heterostructures for THz QCL, as well as the impact of the active region (AR) designs on lasing characteristics. Nowadays, THz QCL is a high power THz source exceeding a peak power of 2 W [176] and CW output power of 200 mW [177]. Moreover, THz QCLs cover a wide frequency range from 1.2 [178] to 5.4 THz [179] and demonstrate a high operating temperature up to 210 K [37], enabling to cool them thermoelectrically under the Peltier effect [180]. Despite significant improvement of the above-mentioned THz QCL parameters, it is necessary to enhance the crystalline quality of heterostructures and develop more efficient designs of AR for advanced THz QCLs.

Basically, contemporary THz QCLs rely on the principle suggested in [181], where the authors have demonstrated the first mid-IR QCL with AR consisting of a multi-period SL with ~ a 100–200–period repetitions (the so-called cascades). Each cascade includes one gain region emitting THz photons and collector/injector regions for the accumulation of electrons from the previous cascade and injecting them into the following one. The necessity of multiple cascade schemes is associated with a small optical gain (g) of intersubband emitters, which is proportional to the product of the dipole matrix element for optical transition (z) and a lifetime of the initial state (τ).

Typical g values for cascade based on intersubband transitions are ~ 50–100 cm^{-1} at low temperatures for polar semiconductors with non-radiation lifetimes τ~1 ps due to the fast electron-optical-phonon scattering [182]. It is worthwhile to note that THz QCL waveguides demonstrate high propagation losses because of the strong absorption of the THz radiation by free carriers, which is proportional to the square of the wavelength [183]. Thus, to achieve the threshold conditions for lasing $g_{th}\Gamma = \alpha_w + \alpha_m$, one should need the high mode confinement factor Γ, as well as low waveguide propagation α_w and mirror α_m losses. To reduce α_w below 20 cm^{-1} at 4.2 K [184], the AR thickness should be more than 10 μm that corresponds to ~ 1000–2000 of individual layers.

The operation principle of THz QCL with a cascade based on three QWs is schematically illustrated in Fig. 13. There are three characteristic states associated with an alignment of electron levels in AR under the applied electric field [185,186],. The first alignment occurs, when the lower injector level 1 and the upper injector level 4′ of the next cascade are aligned, which leads to resonant tunneling of electrons through the lasing double-QWs without THz photon emission followed by a subsequent electron relaxation to the lower injector level 1′ of the next cascade by resonant LO phonon emission (Fig. 13b). As the bias is increased, the laser gain overcomes the total losses that lead to the laser threshold. The second alignment of the lower injector level 1 and the upper laser level 3 occurs, which corresponds to the maximum output power of THz QCL (Fig. 13c). The third state associated with the misalignment of electron levels at further increased bias leads to the end of THz QCL lasing (Fig. 13d).

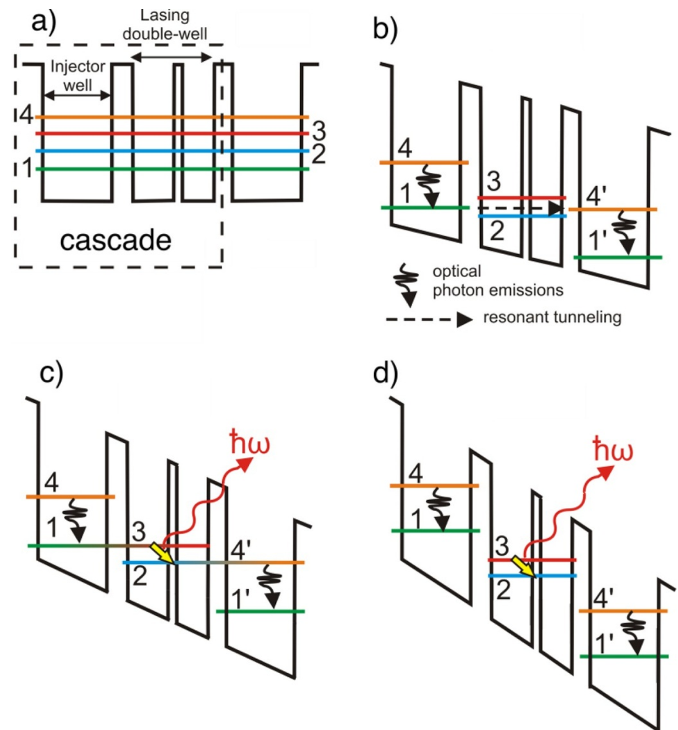

Fig. 13. Energy diagram of AR with a cascade based on three QWs: (a) without electric field, (b) under electric field below the lasing threshold (c) under the electric field for the optimal alignment of electron levels, and (d) under electric field when electron levels are misaligned.

Since the first demonstration of THz QCL based on GaAs/AlGaAs heterostructures [36], a wide variety of materials such as InGaAs/InAlAs [187], InGaAs/GaAsSb [188] and InAs/AlAsSb [189] have been successfully employed for these lasers. The advantage of a low effective mass (m) materials is the higher optical gain due to $z^2 \sim m^{-1}$ and $\tau \sim m^{-1/2}$, then $g \sim m^{-3/2}$. Nevertheless, the technological challenges regarding the growth of the abovementioned materials do not allow for determining the most promising materials for THz QCL, and the evaluation of a material system for these lasers is still under discussion [190]. To date, the most commonly used materials for THz QCLs are multilayered structures based on GaAs/AlGaAs, which will be discussed in this section.

2.1. MBE growth of GaAs/AlGaAs multilayered structures

The operation of THz QCL is strongly dependent on the reproducibility of the QWs and barrier layers with specific thicknesses throughout the epitaxial growth of the AR [191]. Considering the typical MBE growth rate as ~ 1 μm/h [192], the growth time of THz QCL structures exceeds 10 h. This emphasizes the importance of the strict control of the growth rates and the stability of Si and III group effusion cell fluxes during the growth [193,194]. Note that it is necessary to provide a deviation of the AR thickness of less than ±1% in order to achieve emission frequency within ±0.5 THz [195]. The thickness tolerance for lasing heterostructure should be minimally above 2%, while structures with a thickness deviation of 4.3 and 6.5% are not lasing [196].

To ensure the growth of THz QCL structures with an epitaxial window of 1%, accurate calibration of the growth rate and the stability of the effusion cell fluxes during the long growth are essential. For accurate calibration of the growth rate, the X-ray diffraction of short-

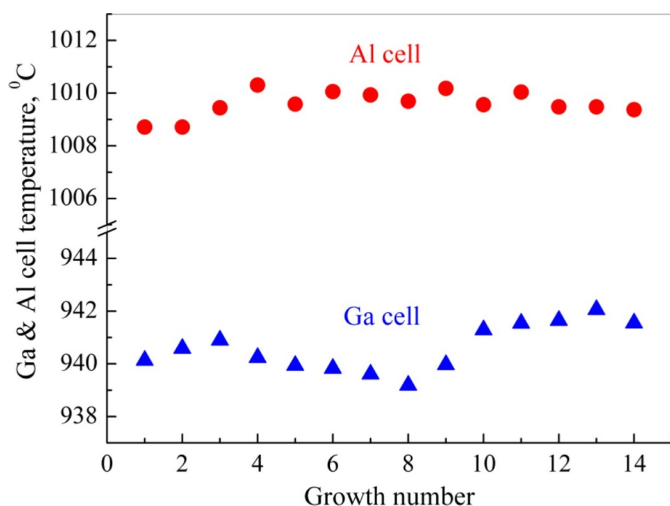

Fig. 14. Dynamics of temperature changes of Al and Ga cells in a series of sequentially grown THz QCL structures using Riber 412 MBE. Adapted with permission from Yu. Sadof'ev.

period SL grown before THz QCL is highly preferable [196,197]. In [193,198] the authors have demonstrated the accuracy even better than 1% using the *in-situ* optical measurements of growth rate during the THz QCL growth.

The investigation of the stability of effusion cell fluxes is performed in [191], where the drift of growth flux for VG Semicon VG80H MBE is less than −0.6% for the gallium cell and less than −0.8% for the aluminum cell during a 12 h growth. In [193] the Ga cell temperature is increased with +0.113 °C/μm to maintain a GaAs constant growth rate while the Al cell temperature is remaining nearly constant due to a variation in AlAs growth rate, which could be neglected. Using such a growth rate compensation technique, the two nominally identical structures exhibiting approximately 10 μm AR thickness have been found to demonstrate a thickness difference of ~1%. However, it is essential to note that the compensation temperature coefficient is unique for each MBE system. In Fig. 14 the variation of Ga and Al cells temperatures is demonstrated in order to obtain the desired growth rate in a series of sequentially grown THz QCL structures using Riber 412 MBE. It is clearly seen that the required change in Ga cell temperature is non-monotonic and differs from the abovementioned value. Thus, calibration procedures and accurate analysis techniques become crucial to provide the required 1% accuracy of the MBE growth for THz QCLs.

Moreover, to control the growth rate and stability of effusion cell flux, it is necessary to take into account the effects of shutter transients. When the mechanical shutters are moving from "open" to "close" positions during the epitaxial growth, a temperature gradient occurs [199]. The latter affects the amount of material flow from the cell and is crucial for the growth of very thin layers. Therefore, one should minimize this effect to improve the quality of THz QCL heterointerfaces.

The influence of interface roughness of GaAs/AlAs QWs grown by MBE on their optical properties was studied using photoluminescence spectroscopy [200]. In order to compare different correlation lengths of the in-plane disorder potential, the QWs were grown with growth interruption at each interface. It is demonstrated that the growth interruption increases the correlation of the monolayer-island structure on the surface, which, consequently, gives rise to a long-range interface roughness after overgrowth. Moreover, when the correlation length of in-plane disorder potential is larger than the exciton localization length, the exciton spectrum splits up into discrete peaks. These peaks are associated with different regions distinguished by an integral number of monolayers. In [201], the authors discuss the influence of the in-band and intersubband scattering caused by interface roughness on the characteristics of the GaAs/AlGaAs-based THz QCLs. It is shown that

Table 2
The influence of growth interruption time on intersubband transition linewidth for normal GaAs/AlGaAs and inverted AlGaAs/GaAs heterointerfaces.

Growth interruption time, s		0	30	60	120
Linewidth, meV	GaAs/AlGaAs interface	8.2	8.8	9.1	9.0
	AlGaAs/GaAs interface		7.3	7.7	7.3
	Both interfaces		–	–	7.7

the introduction of AlAs barriers as well as using of $Al_{0.30}Ga_{0.70}As$ barriers with thin QWs (<30 monolayers) leads to a drastic increase in the linewidth broadening from ~0.66 meV to ~2 meV. Additionally, QWs thinner than 35 monolayers are necessary to suppress thermally activated leakage into the continuum, which has a detrimental effect on THz QCL due to the formation of a negative differential resistance region on a current-voltage characteristic.

It is important to note that the heterointerfaces GaAs/AlGaAs (AlGaAs-on-GaAs) and AlGaAs/GaAs (GaAs-on-AlGaAs) are nonequivalent. Precisely, the inverted interface AlGaAs/GaAs is rougher than normal interface GaAs/AlGaAs, which refers to the diffusion and segregation of atoms towards the growth direction. To achieve smoother interfaces of the inverted AlGaAs/GaAs, one should provide the growth interruption. However, this can have a negative effect on the GaAs/AlGaAs interfaces due to the accumulation of impurities on GaAs surfaces. The authors of [202] investigate the 87-period {GaAs/$Al_{0.33}Ga_{0.67}As$} 8.3/20 nm thick MQWs grown by MBE on semi-insulating GaAs substrate. In fact, a narrowing of intersubband transition linewidth occurs in the structures with interruptions at AlGaAs/GaAs interfaces, and, conversely, a linewidth broadening appears in the structures with interruptions at GaAs/AlGaAs interfaces, as it is shown in Table 2. It should be noted that the same asymmetry of heterointerfaces InAlAs/InGaAs and InGaAs/InAlAs has been demonstrated earlier in the heterostructures for mid-infrared QCL [203]. Nevertheless, the given effect for InAlAs/InGaAs THz QCLs has not been studied properly yet.

A typical image of a cross-sectional dark-field scanning TEM (DF STEM) for two lasing QWs of THz QCL structure based on a resonant-phonon design [186] [204], is depicted in Fig. 15. The interface roughness for this complex heterostructures is about 1 nm, which might be crucial for thin barrier layers. The experimental investigation of the interface profile of GaAs/$Al_{0.25}Ga_{0.75}As$ and GaAs/AlAs THz QCL structures was carried out in [205]. This was the first attempt to quantify the composition profile of THz QCL structures with high Al content in barriers using a combination of Fourier-transform-based simulations and DF TEM. The authors have observed a significant decrease of the Al content in the $Al_{0.25}Ga_{0.75}As$ and AlAs barrier layers compared to the nominal value, which is of great importance for the development of novel design strategies toward a room-temperature THz QCL.

2.2. *Designs of active region*

There are several approaches to achieve population inversion in THz QCLs using different mechanisms of electron injection and extraction. The following mechanisms are used for depopulation of the lower laser level: (1) an electron-electron scattering between the tightly energy-coupled states (bound-to-continuum design, i.e. BTC [206]) and (2) a resonant electron-longitudinal-optical-phonon (LO) scattering (resonant-phonon design [207]). In both designs, resonant tunneling is used to inject electrons into the upper laser level. In the scattering-assisted design [208], the injection of electrons to the upper laser level is based on resonant emission of an optical phonon. It should be noted that there are several excellent reviews dedicated to the AR designs [209–211]; thus, we will consider the following different approaches aimed at the modification of the already known AR designs:

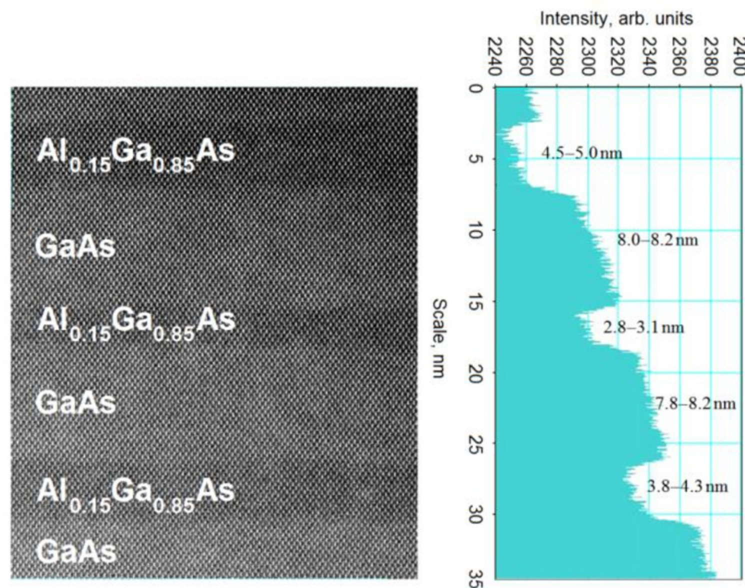

Fig. 15. DF STEM image of two lasing QWs of one cascade of GaAs/$Al_{0.15}Ga_{0.85}As$ THz QCL structure.

i) The variation of AR thickness

The variation of AR thickness can be used for tuning of the emission frequency. In [198], the authors reported on two THz QCLs based on nominally identical $Al_{0.15}Ga_{0.85}As$/GaAs multilayered heterostructures that emit at different frequencies of 2.59 THz and 2.75 THz due to unintentional small deviations in GaAs and AlAs growth rates (4% and 1.6%, respectively). Later it was demonstrated a ~60 GHz blue-shift of the QCL emitting at 2 THz with a 3% thinner AR compared to the reference structure [212]. The other example of AR thickness variation was associated with the calibration error of the Ga flux rate in [174]. This leads to a shift of the gain maximum from 4.8 THz toward 5.3 THz due to a –5.4% thickness deviation of AR as compared to the nominal design. Importantly, the frequency tuning under the increase/decrease in the AR thickness depends on the AR design. Therefore, one should vary the thickness of the cascade layers of the reference design to tune the frequency of THz QCL.

The variation of AR thickness has a great impact on the electrical properties and performance of THz QCL [195]. To minimize the performance degradation of THz QCL, a two-step approach has been proposed [213]. It is based on the scaling of QWs thickness in order to achieve the desired frequency and the modification of barrier layer thickness. The given methodology allows improving the output power characteristics and the maximum operating temperature of THz QCL with a thicker AR. Experimentally it can be realized by the deliberate variation of growth rate. In [214], it was reported on the fabrication of heterogeneous AR by reducing a Ga growth rate systematically to 10% during the MBE growth. This resulted in the ability of dual-frequency emission at ~3.05 THz and ~3.24 THz at different biases which is extremely useful for THz imaging system based on THz QCL.

ii) The variation of doping concentration

The performance of GaAs/$Al_{0.15}Ga_{0.85}As$ THz QCLs as a function of injector doping is investigated in [215]. The authors have demonstrated that both maximum current and threshold currents increase linearly with doping in THz QCL based on the BTC design. In [216], it is shown that optimal doping concentration should be of 3.6×10^{10} cm^{-2} to reach a maximum operating temperature of THz QCL. However, it is clear that the optimal doping depends on the operating frequency as well as the AR design THz QCL. Furthermore, the alternative design approach is suggested in [217], where the space charge region appears after the doping of the injector barrier. This space charge region allows increasing the efficiency of injection by resonant tunneling over a wide range of bias voltages due to the self-alignment of the injector state and the upper laser level. Moreover, the authors of [218] have investigated the influence of dopant migration effects on the performance of THz QCL. It has been proved that the asymmetric distribution of dopants across the structure causes different impurity scattering rates and hence different upper laser level lifetimes/tunneling dephasing times.

iii) The variation of the barrier height

The reasons for cryogenic operation temperature, as well as low wall-plug efficiency of THz QCLs, are associated with a carrier leakage into continuum state at elevated temperatures [219]. It is clear that higher potential barriers with increased Al content in $Al_xGa_{1-x}As$ layers will become beneficial to reduce this parasitic leakage channel. However, it is necessary to reduce the thickness of potentially higher $Al_xGa_{1-x}As$ barriers to maintain efficient electron injection and extraction throughout these barriers. Furthermore, decreasing the thickness of barriers with high Al content creates high requirements on the epitaxial growth in comparison with conventional $Al_{0.15}Ga_{0.85}As$ barriers providing technological maturity.

The study covers the influence of the Al content in barrier layers on lasing characteristics has been performed in [220]. It is shown that THz QCL with 25% of Al content has significantly lower threshold current density as compared to the one with 15% of Al content. Recently, in [221], the authors have analyzed the THz QCL structures with identical AR designs and various barrier heights for different Al concentration from 12% to 24%. A record operating temperature of 196 K for the emission frequency of 3.8 THz has been obtained for the structure with 21% of Al in barrier layers. In [222], it is demonstrated the THz QCL with AlAs barriers exhibiting higher wall-plug efficiency and lower threshold current density compared to THz QCL with $Al_{0.25}Ga_{0.75}As$ barriers with an identical AR design. Alternatively to the above-mentioned studies, in [223], the authors suggest using short barriers with 10% of Al content for lowering current density in THz QCL. This approach can be explained as the decreasing of interface-roughness scattering in the structures with thicker barrier layers.

iv) The heterogeneous AR

One of the approaches for the development of ultra-broadband THz QCL is based on the stacking of different AR designs into a common waveguide. The authors in [224] reported on a heterogeneous THz QCL that emits broadband radiation between 2.2 THz and 3.2 THz. This is achieved by stacking of three different AR designs with center frequencies of 3 THz, 2.7 THz, and 2.3 THz to obtain a flat gain medium for desired bandwidth. Based on a similar approach, in [225] the authors proposed a THz QCL with an emission spanning more than one octave from 1.64 THz to 3.35 THz. The octave-spanning laser emission allows for stabilizing a frequency comb using the “self-referencing” *f*–2*f* method [226] for the widespread use of THz QCLs in metrology and high-precision spectroscopy. Later a double comb source based on heterogeneous THz QCL has been demonstrated in [227]. The heterogeneous AR is comprised of 120 cascades with 2.3 THz central frequency and 80 cascades with 4.6 THz central frequency that provides a simultaneous presence of two octave-spaced combs. A heterogeneous AR approach allows for fabricating a broadband THz amplifier with amplification over a 500 GHz-bandwidth with an amplification factor of 21 dB centered at 2.47 THz [228].

3. Structures exhibiting negative differential conductivity

In this section, we consider the multilayered structures with specific transport when the electron current spreads from the bottom of the structure to its top. The uncooled SL-based diodes, as well as the RTDs based on these structures, demonstrate the negative differential conductivity region on its I-V curve. The RTDs are usually implemented as THz emitters based on fundamental self-oscillations, while the SL diodes are mostly used as frequency multipliers converting the external GHz signal to the THz one.

3.1. Double-barrier and triple-barrier structures for resonant-tunneling diodes

In the double-barrier RTD, the resonant tunneling of electrons occurs between the conduction band electron states and the confined electron state in the QW. The general design of the double-barrier RTD structure is shown in Fig. 16. The InP wafer can be either *n*-type or isolate; in both cases, a highly *n*-doped bottom contact layer is necessary.

The THz radiation is generated when the DC-biased diode is connected to the resonant circuit. The RTD oscillators are similar to the THz QCLs with the active part just of a single period. On the contrary to the THz QCL, the RTD is a room-temperature oscillator. The RTD operated in the non-linear positive differential conductivity region of its *I*-*V* curve is able to detect the THz radiation with quite high frequency (up to 3.9 THz [230]), and for this aim, it must be combined with either non-resonant broadband or resonant antenna [231].

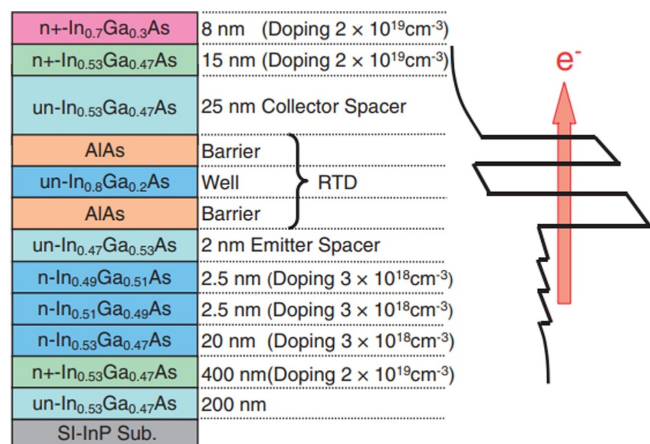

Fig. 16. Layout of double-barrier RTD structure with its potential profile. From H. Kanaya, H. Shibayama, R. Sogabe, S. Suzuki, M. Asada, Appl. Phys. Express 5 (2012) 124101. Copyright (2012) The Japan Society of Applied Physics [238].

The theoretical and experimental results for sub-THz and THz oscillators with the RTDs integrated on planar circuits (until 2008) are thoroughly described in [232]. Later, different authors have gradually increased the radiation frequency of the RTDs from 0.83 THz to 1.92 THz by improving the RTD's structure and the antenna design. In Table 3, we summarized the progress mainly in the upper limit of the achieved frequency range of the RTD oscillators. Their output power in the last years has been steadily increased, approaching the mW at the frequencies close to 1 THz [231].

Note that despite the RTD oscillators are usually exploited at room temperature, some studies have been focused on how the oscillation frequency, as well as the output power, will alter at cryogenic temperature. It was recently shown that the output THz power could be increased owing to the decrease of Ohmic losses while the oscillation frequency and the I-V characteristic were almost insensitive to the temperature [233,234].

On the contrary to the double-barrier RTD, the triple-barrier RTD allows for suppressing the energy broadening of impinging electrons and consequently, the broadening of current peaks on the I-V characteristic [244]. The authors in [239] reported on the triple-barrier RTD-oscillator based on two QWs separated by three barrier layers AlAs/i-$In_{0.53}Ga_{0.47}As$/i-$In_{0.52}Al_{0.48}As$/i-$In_{0.53}Ga_{0.47}As$/AlAs with thicknesses of 1.3/7.6/2.6/5.6/1.3 nm respectively, grown on a *n*-type InP wafer. It was shown that using the integrated patch antenna, the RTD can cover the wide frequency range starting from 1.02 THz to 1.40 THz.

3.2. Superlattices for frequency multipliers, autocorrelators, and sub-THz emitters

The GaAs/AlAs SL demonstrate the negative differential conductivity region in the direction perpendicular to the growth plane of the SL. This feature, firstly predicted by L. Esaki, is caused by the Bragg reflections of conduction electrons in the SL's miniband [245]. The 120-period SL consisted of a 3.63 nm-thick GaAs layer, and a 1.17 nm-thick AlAs layer was used in experimental investigations [246]. The operation principle is based on the THz radiation-induced current reduction through the SL, which can resolve free-electron laser pulses with the frequency of 7.2 THz featuring a few picoseconds duration. The authors suggested that the limit for the temporal resolution of the SL-based autocorrelator is related to the intraminiband relaxation time of 100 fs. The authors of [247] reported on the GaAs/AlAs wide-miniband SL autocorrelator for the generation of the THz pulses.

Thanks to the nonlinearity of the I-V or C-V characteristics (see Fig. 17), the SL-based diodes act as frequency multipliers based on harmonics generation: these devices can convert the GHz-frequency ac-voltage to the THz-frequency ac-current. When the SL-based diode with such I–V characteristic is subjected to a sinusoidal voltage with an amplitude exceeding some critical value, the non-sinusoidal current through the diode is observed, including the excitation of higher harmonics. Compared to the Schottky barrier diodes, the SL-based diodes provide shorter response times and less parasitic capacitances [248]. Thereby the SL-based diodes are more suitable to generate the THz signals by multiplying the intense ones with the moderate GHz frequencies, while the Schottky barrier diodes require relatively high input frequencies with elevated input powers to attain the THz frequency range [249].

The authors in [249] have studied the 112 nm thick 18-period SLs, which were grown on a semi-insulating GaAs wafer. Each period included 18 monolayers of GaAs and 4 monolayers of AlAs corresponding to the period thickness of 6.22 nm. The SLs were doped with the donor concentration of 10^{18} cm^{-3}. The input frequency of 0.25 THz from a backward wave oscillator with the average power of 10–60 mW was multiplied up to the 11th harmonic, producing the frequency of

Table 3
The progress in characteristics of RTD oscillators.

Oscillation frequency, THz	Output power, μW	Specific features of the RTD oscillators	Ref.
0.52	0.01	Two QWs separated by three $AlAs/In_{0.53}Ga_{0.47}As/In_{0.52}Al_{0.48}As/In_{0.53}Ga_{0.47}As/AlAs$ barrier layers with thicknesses of 1.3/7.6/2.6/5.6/1.3 nm. The integrated patch antenna is used.	[235]
0.83	~1	Double-barrier RTD structure with QW $AlAs/In_{0.8}Ga_{0.2}As/AlAs$ (1.4/4.5/1.4 nm). The uniform emitter (with spacer) i-$In_{0.53}Ga_{0.47}As$/n-$In_{0.53}Ga_{0.47}As$ (2/25 nm) and the collector spacer layer n-$In_{0.53}Ga_{0.47}As$ (25 nm). The 20 μm length slot antenna is used.	[229]
1.04	7	Graded emitter (with spacer) i-$In_{0.47}Ga_{0.53}As$/n-$In_{0.49}Ga_{0.51}As$/n-$In_{0.51}Ga_{0.49}As$/n-$In_{0.53}Ga_{0.47}As$ (2.0/2.5/2.5/20 nm) is employed to reduce the electric field in the collector depletion layer, which resulted in the suppression of the Γ–L valley electron scattering and the decrease of the transit time in the collector depletion region. Thin barrier layers AlAs (1.2 nm) allow reducing the resonant tunneling time.	[236]
1.11	0.1	Composite QW $In_{0.53}Ga_{0.47}As/InAs/In_{0.53}Ga_{0.47}As$ (1.2/1.2/1.2 nm) sandwiched between 1.2 nm AlAs barrier layers. The slot antenna is used.	[237]
1.31	10	The decrease of $In_{0.80}Ga_{0.20}As$ QW (3.9 nm) and AlAs barrier layer (1.0 nm) thicknesses in order to reduce dwell time in the resonance region.	[238]
1.40	0.01	Two QWs separated by three barrier layers $AlAs/In_{0.53}Ga_{0.47}As/In_{0.52}Al_{0.48}As/In_{0.53}Ga_{0.47}As/AlAs$ with thicknesses of 1.3/7.6/2.6/5.6/1.3 nm. The integrated patch antenna is used. The mesa structure and the length of the antenna are improved.	[239]
1.42	~1	Optimized thickness of $In_{0.53}Ga_{0.47}As$ collector spacer layer (12 nm instead of 25 nm) due to the decrease in transit time in collector depletion region and the increase of collector depletion region capacitance.	[240]
1.55	0.4	Optimized slot antenna length (16 μm instead of 20 μm).	[241]
1.86	0.03	The decrease of the QW thickness (2.5 nm instead of 3.0 nm) and the use of 1 μm air-bridge between RTD mesa and antenna.	[242]
1.52	1.9	Composite QW $In_{0.53}Ga_{0.47}As/InAs/In_{0.53}Ga_{0.47}As$ (1/1/1 nm) sandwiched between 1.2 nm AlAs barrier layers, a triple-push oscillator with patch antenna.	[243]
1.92	0.4	Removal of n^+-$In_{0.53}Ga_{0.47}As$ layer under the air-bridge electrode to reduce significant conduction losses for high-frequency current due to skin effect.	[38]

2.7 THz.

The SL-based diodes are also able to generate current self-oscillations that nevertheless occur at sub-THz frequencies due to large transit time for the propagation of a domain from cathode to anode through the thick SL. The output power, as well as the conversion efficiency of the SL-based diodes, is considered to be higher than those for the RTDs at similar frequencies [250].

Later in [251], the SL-based frequency multiplier was subjected to the input voltage signal of 0.14–0.16 THz and the power of 5–15 mW from frequency synthesizer with negligible intensities of inherent harmonics. It was shown that a more significant portion of the output signal is contained in the first 10 harmonics that occupy the frequency range up to 1.5 THz.

In [252] the authors proposed a room temperature sub-THz generator based on the 110-period GaAs/AlAs SL. It consisted of GaAs and AlAs layers with thicknesses of 11–12 MLs and 2 MLs, respectively, with the Si-doping concentration in the range of (1.5–1.8) × 10^{17} cm^{-3}. The SL was sandwiched between the graded transition layers on both sides. Then, a 0.5 μm thick $Al_{0.55}Ga_{0.45}As$ layer was used between the substrate and the SL, allowing a complete wafer removal during the device fabrication. The lower 30 nm thick graded layer consisted of alternating GaAs sublayers with a constant thickness of 11 MLs and AlAs sublayers with thickness increasing from 1 to 7 MLs. They ensured a continuous transition from the band structure of the GaAs to that of the GaAs/AlAs SL, avoided quasi-heterojunctions, and provided a smooth carrier injection into the SL. To improve crystal perfection, the growth was interrupted at each AlAs/GaAs interface for 5 s. The structural parameters were studied by X-ray scattering (Bragg diffraction, specular, and diffuse scattering methods) and resulted in the fluctuation of SL period ~ 1 ML, the interface roughness ~ 1 ML, the lateral correlation length ~ 100 nm. Note that such interface roughness might be responsible for elastic scattering of the miniband electrons at a rate ~ 10^{13} s^{-1}. The proposed sub-THz generator yielded output signals in the fundamental mode between 0.105 THz and 0.175 THz and in the second harmonic mode with a frequency of 0.32 THz.

Theoretically, the SL-based diode is able to produce only odd harmonics, but in a real case, the SLs, due to its rough interfaces, can demonstrate additional even harmonic response. The special designs of the SL interface imperfections may contribute to the efficient controlling of GHz-to-THz conversion efficiency for even harmonics,

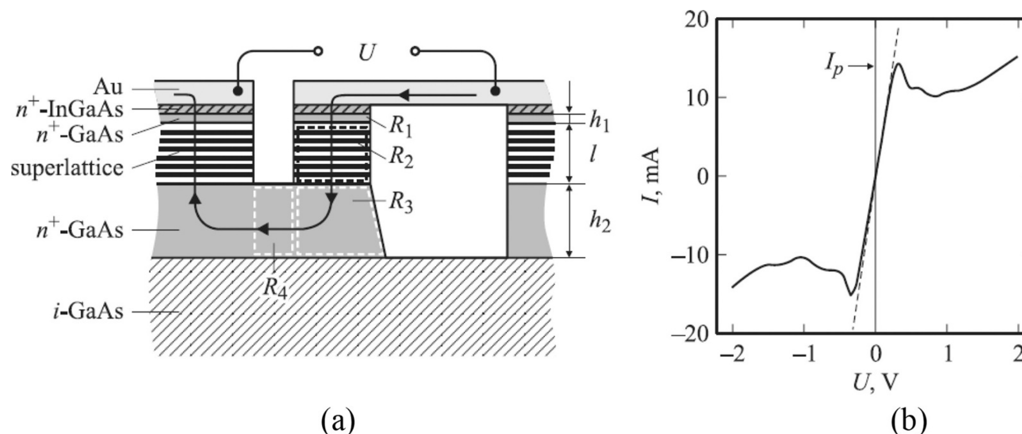

Fig. 17. Layout of GaAs/AlAs SL-based planar diode (a) and its I-V characteristic (b). Adapted with permission from [248].

expanding the frequency range of the SL-based multipliers [253]. The features of normal and inverse heterointerfaces GaAs/AlGaAs, as well as technological methods affecting the parameters of heterointerface roughness during the MBE growth, were discussed earlier for the QCLs in Section 2.

In conclusion, we note that theoretically predicted DC-biased coherent THz generator based on the Bloch oscillations with weak SLs barrier [245] (i.e. an inversionless CW laser tunable by an electric field) isn't still fulfilled owing to rising and traveling space charge domains which oscillate with GHz frequency [246,254]. Interestingly, T. Unuma et al. in [255,256] demonstrated the room-temperature 2. THz gain of Bloch oscillations in the biased undoped GaAs/AlAs (7.5/0.5 nm) SL grown by MBE on a Si-doped (001) GaAs substrate (the electron concentration in SL was kept as low as 2×10^{14} cm^{-3}). However, these Bloch oscillations are rapidly damping while their dephasing time is governed by elastic scattering mainly on interface roughness and negligibly on alloy disorder. In [257], the same authors demonstrated that the relaxation time of Bloch oscillations is governed by interface roughness scattering at low temperatures and becomes shorter with increasing temperature owing to the phonon scattering.

Conclusions

In this review, we have briefly summarized important developments in the area of multilayered arsenides-and related III-V materials-based structures that are used as base materials in modern sub-THz and THz emitters and detectors. Depending on the operation principle, various designs of the multilayered structures are required with thus stimulating the fabrication of new functional layers to fulfill rapidly-growing demands on their complexity.

We considered different multilayered arsenides-and related III-V materials-based structures as well as their quantum engineering, designs, and operation principle. In particular, we discussed:

- (In)GaAs-based superlattices with lattice-matched and strained functional layers featuring different kinds of trapping regions and used for photoconductive THz emitters and detectors, as well as structures with *p-i-n* design;
- GaAs/Al(Ga)As-based superlattices for THz quantum-cascade lasers;
- (In)AlAs/InGaAs/(In)AlAs double-barrier and triple-barrier structures for THz-oscillators based on resonant-tunneling diodes and the SL-based diodes.

We made an emphasis on the designs and physical interpretation of the mechanisms of THz emission and detection using the above-mentioned multilayered structures. We qualitatively divided the structures depending on the composition, excitation wavelength, THz coupling, as well as the operating temperature of the fabricated devices.

There is no doubt that the widely used multilayered arsenides-and related III-V materials-based structures will further provide important fundamental and practical applications at the forefront of scientific knowledge (sensors, flexible electronics, security systems, biomedicine, and others) due to permanently growing interest in the THz field applications, thus encouraging research aimed at the development of new multilayered designs and the improvement of their growth technology.

Acknowledgments

This paper was supported by the Russian Science Foundation (RSF). The work of A.E. Yachmenev and R.A. Khabibullin on section I on binary and ternary compounds was supported by the RSF grant #19-79-10240. The work of D.S. Ponomarev on section I on photoconductive antennas was supported by the RSF grant #18-79-10195. The work of R.R. Reznik and D.S. Ponomarev on section II was supported by the RSF, grant #18-19-00493. The work on section III was supported by the Russian Foundation for Basic Research, grant #20-32-70129 mol_a_ved.

We also sincerely thank Profs. K. Zaytsev and V. Kurlov for their valuable discussions on the improvement of the manuscript.

References

[1] H. Rubens, E. Nichols, Phys. Rev. (Series I) 4 (1897) 314.
[2] H. Rubens, F. Kurlbaum, Astrophys. J. 14 (1901) 335–348.
[3] Y.-S. Lee, Principles of Terahertz Science and Technology, Springer, 2009.
[4] R. Ulbricht, E. Hendry, J. Shan, T. Heinz, M. Bonn, Rev. Mod. Phys. 83 (2) (2011) 543–586.
[5] C. Cervetti, E. Heintze, B. Gorshunov, E. Zhukova, S. Lobanov, A. Hoyer, M. Burghard, K. Kern, M. Dressel, L. Bogani, Adv. Mater. 27 (16) (2015) 2635–2641.
[6] J. Buron, D. Petersen, P. Boggild, D. Cooke, M. Hilke, J. Sun, E. Whiteway, P. Nielsen, O. Hansen, A. Yurgens, P. Jepsen, Nano Lett. 12 (10) (2012) 5074–5081.
[7] R. Jacobsen, D. Mittleman, M. Nuss, Opt. Lett. 21 (24) (1996) 2011–2013.
[8] B. Fischer, M. Hoffmann, H. Helm, G. Modjesch, P. Uhd Jepsen, Semicond. Sci. Technol. 20 (7) (2005) 246–253.
[9] P. Taday, Phil. Trans. R. Soc. A. 362 (1815) (2004) 351–363.
[10] J. Zeitler, P. Taday, D. Newnham, M. Pepper, K. Gordon, T. Rades, J. Pharm. Pharmacol. 59 (2) (2007) 209–223.
[11] K. Kawase, Y. Ogawa, Y. Watanabe, H. Inoue, Opt. Express 11 (20) (2003) 2549–2554.
[12] I. Dolganova, K. Zaytsev, A. Metelkina, V. Karasik, S. Yurchenko, Rev. Sci. Instrum. 86 (11) (2015) 113704.
[13] K. Ahi, IEEE Trans. Terahertz Sci. Technol. 7 (6) (2017) 747–754.
[14] X. Yang, X. Zhao, K. Yang, Y. Liu, Y. Liu, W. Fu, Y. Luo, Trends Biotechnol. 34 (10) (2016) 810–824.
[15] Q. Sun, Y. He, K. Liu, S. Fan, E. Parrott, E. Pickwell-MacPherson, Quant. Imaging Med. Surg. 7 (3) (2017) 345–355.
[16] D. Auston, Appl. Phys. Lett. 26 (3) (1975) 101–103.
[17] A. Jooshesh, F. Fesharaki, V. Bahrami-Yekta, M. Mahtab, T. Tiedje, T.E. Darcie, R. Gordon, Opt. Express 25 (18) (2017) 22140.
[18] N.T. Yardimci, M. Jarrahi, Sci. Rep. 7 (2017) 42667.
[19] M. Mikulics, M. Marso, I. Cámara Mayorga, R. Güsten, S. Stanček, P. Kováč, S. Wu, Xia Li, M. Khafizov, R. Sobolewski, E.A. Michael, R. Schieder, M. Wolter, D. Buca, A. Förster, P. Kordoš, H. Lüth, Appl. Phys. Lett. 87 (2005) 041106.
[20] M. Mikulics, E.A. Michael, M. Marso, M. Lepsa, A. van der Hart, H. Lüth, A. Dewald, S. Stanček, M. Mozolik, P. Kordoš, Appl. Phys. Lett. 89 (2006) 071103.
[21] M. Koch, D. Weber, J. Feldmann, E.O. Göbel, T. Meier, A. Schulze, P. Thomas, S. Schmitt-Rink, K. Ploog, Phys. Rev. B. 47 (1993) 1532–1539.
[22] N.T. Yardimci, D. Turan, S. Cakmakyapan, M. Jarrahi, Appl. Phys. Lett. 113 (2018) 251102.
[23] C. Kadow, A.W. Jackson, A.C. Gossard, J.E. Bowers, S. Matsuura, G.A. Blake, Physica E Low dimens. Syst. Nanostruct. 7 (1–2) (2000) 97–100.
[24] E. Estacio, M. Hong Pham, S. Takatori, M. Cadatal-Raduban, T. Nakazato, T. Shimizu, N. Sarukura, A. Somintac, M. Defensor, F.C.B. Awitan, R.B. Jaculbia, A. Salvador, Alipio Garcia, Appl. Phys. Lett. 94 (2009) 232104.
[25] F. Ospald, D. Maryenko, K. von Klitzing, D.C. Driscoll, M.P. Hanson, H. Lu, A.C. Gossard, J.H. Smet, Appl. Phys. Lett. 92 (2008) 131117.
[26] N.T. Yardimci, S. Cakmakyapan, S. Hemmati, M. Jarrahi, Sci. Rep. 7 (2017) 4166.
[27] R.J.B. Dietz, B. Globisch, M. Gerhard, A. Velauthapillai, D. Stanze, H. Roehle, M. Koch, T. Gobel, M. Schell, Appl. Phys. Lett. 103 (2013) 061103.
[28] D.S. Ponomarev, A. Gorodetsky, A.E. Yachmenev, S.S. Pushkarev, R.A. Khabibullin, M.M. Grekhov, K.I. Zaytsev, D.I. Khusyainov, A.M. Buryakov, E.D. Mishina, J. Appl. Phys. 125 (2019) 151605.
[29] E.R. Brown, A. Mingardi, W.-.D. Zhang, A.D. Feldman, T.E. Harvey, R.P. Mirin, Appl. Phys. Lett. 111 (3) (2017) 031104.
[30] A. Mingardi, W.-.D. Zhang, E.R. Brown, A.D. Feldman, T.E. Harvey, R.P. Mirin, Opt. Express 26 (2018) 14472–14478.
[31] R.R. Leyman, A. Gorodetsky, N. Bazieva, G. Molis, A. Krotkus, E. Clarke, E.U. Rafailov, Laser Photonics Rev. 10 (2016) 772–779.
[32] K.A. Fedorova, A. Gorodetsky, E.U. Rafailov, IEEE J. Sel. Top. Quantum Electron. 23 (4) (2017) 1–5.
[33] C. Kadow, S.B. Fleischer, J.P. Ibbetson, J.E. Bowers, A.C. Gossard, J.W. Dong, C.J. Palmstrom, Appl. Phys. Lett. 75 (1999) 3548.
[34] R.J.B. Dietz, M. Gerhard, D. Stanze, M. Koch, B. Sartorius, M. Schell, Opt. Express 19 (27) (2011) 25911–25917.
[35] N.T. Yardimci, R. Salas, E.M. Krivoy, H.P. Nair, S.R. Bank, M. Jarrahi, Opt. Express 23 (25) (2015) 32035–32043.
[36] R. Kohler, A. Tredicucci, F. Beltram, H.E. Beere, E.H. Linfield, A.G. Davies, D.A. Ritchie, R.C. Iotti, F. Rossi, Nature 417 (2002) 156–159.
[37] L. Bosco, M. Franckie, G. Scalari, M. Beck, A. Wacker, J. Faist, Appl. Phys. Lett. 115 (2019) 010601.
[38] T. Maekawa, H. Kanaya, S. Suzuki, M. Asada, Appl. Phys. Express 9 (2016) 024101.
[39] M.S. Vitiello, G. Scalari, B. Williams, P.D. Natale, Opt. Express 23 (4) (2015) 5167.
[40] N.M. Burford, M.O. El-Shenawee, Opt. Eng. 56 (1) (2017) 010901.
[41] S. Lepeshov, A. Gorodetsky, A. Krasnok, E. Rafailov, P. Belov, Laser Photonics Rev. (2017) 1600199.
[42] A.E. Yachmenev, D.V. Lavrukhin, I.A. Glinskiy, N.V. Zenchenko, Y.G. Goncharov, I.E. Spektor, R.A. Khabibullin, T. Otsuji, D.S. Ponomarev, Opt. Eng. 59 (6) (2019) 061608.

[43] A. Krotkus, J. Phys, D Appl. Phys. 43 (2010) 273001.
[44] S. Gupta, M.Y. Frankel, J.A. Valdmanis, J.F. Whitaker, G.A. Mourou, F.W. Smith, A.R. Calawa, Appl. Phys. Lett. 59 (25) (1991) 3276.
[45] J.K. Luo, H. Thomas, D.V. Morgan, D. Westwood, J. Appl. Phys. 79 (7) (1996) 3622.
[46] N. Zamdmer, Q. Hu, K.A. Mclntosh, S. Verghese, Appl. Phys. Lett. 75 15 (1999) 2313.
[47] Y. Kamo, Sh. Kitazawa, S. Ohshima, Yasuo Hosoda, Jpn. J. Appl. Phys. 53 (2014) 032201.
[48] P. Kordoš, A. Förster, M. Marso, F. Rüders, Electron. Lett. 34 (1998) 119.
[49] M. Tani, S. Matsuura, K. Sakai, S. Nakashima, Appl. Optics 36 (30) (1997) 7853–7859.
[50] S. Matsuura, M. Tani, K. Sakai, Appl. Phys. Lett. 70 (1997) 559–561.
[51] S. Matsuura, G.A. Blake, R.A. Wyss, J.C. Pearson, C. Kadow, A.W. Jackson, et al., Appl. Phys. Lett. 74 (1999) 2872–2874.
[52] E.R. Brown, Int. J. High Speed Electron Syst 13 (2003) 497–545.
[53] D.H. Auston, A.M. Johnson, P.R. Smith, J.C. Bean, Appl. Phys. Lett. 37 (4) (1980) 371–373.
[54] D.H. Auston, K.P. Cheung, P.R. Smith, Appl. Phys. Lett. 45 (3) (1984) 284–286.
[55] M.Y. Frankel, J.F. Whitaker, G.A. Mourou, F.W. Smith, A.R. Calawa, IEEE Trans. Electron. Dev. 37 (12) (1990) 2493–2497.
[56] K.A. McIntocsh, E.R. Brown, K.B. Nichols, O.B. McMahon, W.F. Dinatale, T.M. Lyszczarz, Appl. Phys. Lett. 67 (26) (1995) 3844.
[57] E.R. Brown, K.A. McIntosh, K.B. Nichols, C.L. Dennis, Appl. Phys. Lett. 66 (1995) 285–287.
[58] S. Verghese, K.A. McIntosh, E.R. Brown, Appl. Phys. Lett. 71 (1997) 2743–2745.
[59] D.J. Eaglesham, L.N. Pfeiffer, K.W. West, D.R. Dykaar, Appl. Phys. Lett. 58 (1991) 65.
[60] Z. Liliental-Weber, W. Swider, K.M. Yu, J. Kortright, Appl. Phys. Lett. 58 (19) (1991) 2153.
[61] Z. Liliental-Weber, H.J. Cheng, S. Gupta, J. Whitaker, K. Nichols, F.W. Smith, J. of Electronic Mater. 22 (1993) 1465.
[62] J.-.F. Roux, J.-L. Coutaz, A. Krotkus, Appl. Phys. Lett. 74 (1999) 2462.
[63] T.-A. Liu, M. Tani, C.-L. Pan, J. Appl. Phys. 93 (2003) 2996–3001.
[64] P. Deshmukh, M. Mendez-Aller, A. Singh, S. Pal, S.S. Prabhu, V. Nanal, R.G. Pillay, G.H. Döhler, S. Preu, Opt. Letters 40 (2015) 4540.
[65] J. Mangeney, J. Infrared Millim, Teraherz Waves 33 (2012) 455–473.
[66] D.C. Look, Thin Solid Films 231 (1993) 61–73.
[67] D.S. Ponomarev, D.V. Lavrukhin, A.E. Yachmenev, R.A. Khabibullin, I.E. Semenikhin, V.V. Vyurkov, M. Ryzhii, T. Otsuji, V. Ryzhii, J. Phys. D Appl. Phys. 51 (2018) 135101.
[68] D.S. Ponomarev, D.V. Lavrukhin, A.E. Yachmenev, R.A. Khabibullin, I. Semenikhin, V. Vyurkov, K.I. Marem'yanin, V.I. Gavrilenko, M. Ryzhii, M. Shur, T. Otsuji, V. Ryzhii, J. Phys. D Appl. Phys. 53 (2020) 075102.
[69] A. Jackson, Low-temperature-grown Gaas Photomixers Designed For Increased Teraherz Output Power, Ph.D. thesis University of California, Santa Barbara, 1999.
[70] I.C. Mayorga, M. Mikulics, A. Schmitz, P.V. der Wal, R. Gusten, M. Marso, P. Kordos, H. Luth, Proc. SPIE (2004) 5498.
[71] J.E. Bjarnason, T.L.J. Chan, A.W.M. Lee, E.R. Brown, Appl. Phys. Lett. 85 (2004) 3983.
[72] M. Mikulics, S. Wu, M. Marso, R. Adam, A. Forster, A. van der Hart, et al., IEEE Photonics Technol. Lett. 18 (2006) 820–822.
[73] M. Mikulics, M. Marso, S. Wu, A. Fox, M. Lepsa, D. Grutzmacher, et al., IEEE Photonics Technol. Lett. 20 (2008) 1054–1056.
[74] Z.D. Taylor, E.R. Brown, J.E. Bjarnason, M.P. Hanson, A.C. Gossard, Opt. Lett. 31 (2006) 1729–1731.
[75] Y. Wang, I. Kostakis, D. Saeedkia and M. Missous, I.E.T. Optoelectron. 112 (2017) 53–57.
[76] E.R. Brown, Appl. Phys. Lett. 75 (1999) 769.
[77] M. Mikulics, F. Siebe, A. Fox, M. Marso, A. Forster, H. Stuer, et al., Fourth Int. Conf. Adv. Semicond. Devices Microsyst. IEEE (2002) 129–132.
[78] J. Darmo, T. Muller, G. Strasser, K. Unterrainer, G. Tempea, Electron. Lett. 39 (5) (2003) 460–462.
[79] O. Mitrofanov, I. Brener, T.S. Luk, J.L. Reno, ACS Photonics 2 (12) (2015) 1763.
[80] M. Bashirpour, S. Ghorbani, M. Kolahdouz, M. Neshat, M. Masnadi-Shiraziand, H. Aghababa, RSC Adv. 7 (2017) 53010.
[81] J. Darmo, T. Müller, G. Strasser, K. Unterrainer, T. Le, A. Stingl, G. Tempea, Opt. Lett. 27 (2002) 1941–1943.
[82] J. Darmo, R. Bratschitsch, T. Müller, R. Kersting, G. Strasser, K. Unterrainer, Phil. Trans. R. Soc. Lond. A 362 (2004) 251–262.
[83] G. Matthäus, B. Ortaç, J. Limpert, S. Nolte, R. Hohmuth, M. Voitsch, W. Richter, B. Pradarutti, A. Tünnermann, Appl. Phys. Lett. 93 (2008) 261105.
[84] N.S. Wingreen, C.A. Stafford, IEEE J. Quantum Electron. 33 (7) (1997) 1170–1173.
[85] C.-.F. Hsu, J.-.S. O, P. Zory, D. Botez, IEEE J. Sel. Top. Quantum Electron. 6 (3) (2000) 491–503.
[86] T. Sands, C.J. Palmstrom, J.P. Harbison, V.G. Keramidas, N. Tabatabaie, T.L. Cheeks, R. Ramesh, Y. Silberberg, Mater. Sci. Rep. 5 (3) (1990) 99–170.
[87] C. Kadow, J.A. Johnson, K. Kolstad, J.P. Ibbetson, A.C. Gossard, J. Vac. Sci. Technol. B 18 (2000) 2197.
[88] S. Sethi, P.K. Bhattacharya, J. Electron. Mater. 25 (3) (1996) 467–477.
[89] C. Kadow, A.W. Jackson, A.C. Gossard, S. Matsuura, G.A. Blake, Appl. Phys. Lett. 76 (2000) 3510.
[90] J.F. O'Hara, J.M.O. Zide, A.C. Gossard, A.J. Taylor, R.D. Averitt, Appl. Phys. Lett. 88 (2006) 251119.
[91] E.M. Krivoy, H.P. Nair, A.M. Crook, S. Rahimi, S.J. Maddox, R. Salas, D.A. Ferrer, V.D. Dasika, D. Akinwande, S.R. Bank, Appl. Phys. Lett. 101 (2012) 141910.
[92] S.-.H. Yang, R. Salas, E.M. Krivoy, H.P. Nair, S.R. Bank, M. Jarrahi, J. Infrared Millim, Terahertz Waves 37 (2016) 640–648.
[93] J.R. Middendorf, E.R. Brown, Opt. Express 20 15 (2012) 16504–16509.
[94] M. Martin, E.R. Brown, Proc. SPIE (2015) 936207.
[95] W. Zhang, E.R. Brown, A. Mingardi, R.P. Mirin, N. Jahed, D. Saeedkia, Appl. Sci. 9 (15) (2019) 3014.
[96] D. Leonard, M. Krishnamurthy, C.M. Reaves, S.P. Denbaars, P.M. Petroff, Appl. Phys. Lett. 63 (1993) 3203.
[97] J.M. Moison, F. Houzay, F. Barthe, L. Leprince, Appl. Phys. Lett. 64 (1994) 196.
[98] D. Leonard, K. Pond, P.M. Petroff, Phys. Rev. B 50 (1994) 11687.
[99] J.Y. Marzin, J.M. Gerard, A. Izrael, D. Barrier, Phys. Rev. Lett. 73 (1994) 716.
[100] C. Priester, M. Lannoo, Phys. Rev. Lett. 75 (1995) 93.
[101] G.S. Solomon, J.A. Trezza, J.S. Harris Jr., Appl. Phys. Lett. 66 (1995) 991.
[102] L. Chu, M. Arzberger, G. Bohm, G. Abstreiter, J. Appl. Phys. 85 (1999) 2355.
[103] J. Wu, P. Jin, Front. Phys. 10 (2015) 7–58.
[104] E.U. Rafailov, M.A. Cataluna, W. Sibbett, Nat. Photon. 1 (2007) 395–401.
[105] H. Park, J. Kim, K. Moon, H. Han, W.J. Choi, J.I. Lee, 31st International Conference on Infrared Millimeter Waves and 14th International Conference on Teraherz Electronics, 2006, p. 543.
[106] E.U. Rafailov, S.J. White, A.A. Lagatsky, A. Miller, W. Sibbett, D.A. Livshits, A.E. Zhukov, V.M. Ustinov, IEEE Photon. Technol. Lett. 16 (2004) 2439.
[107] H.P. Porte, P. Uhd Jepsen, N. Daghestani, E.U. Rafailov, D. Turchinovich, Appl. Phys. Lett. 94 (26) (2009) 262104.
[108] N.S. Daghestani, M.A. Cataluna, G. Berry, G. Ross, M.J. Rose, Phys. Status Solidi C 9 (2012) 222–225.
[109] T. Kruczek, R. Leyman, D. Carnegie, N. Bazieva, G. Erbert, S. Schulz, C. Reardon, S. Reynolds, E.U. Rafailov, Appl. Phys. Lett. 101 (2012) 081114.
[110] A. Gorodetsky, N. Bazieva, E.U. Rafailov, J. Appl. Phys. 125 (2019) 151606.
[111] C. Berry, M. Hashemi, S. Preu, H. Lu, A. Gossard, M. Jarrahi, Opt. Lett. 39 (15) (2014) 4522–4524.
[112] S. Preu, G. Döhler, S. Malzer, L. Wang, A. Gossard, J. Appl. Phys. 109 (6) (2011) 061301.
[113] A. Takazato, M. Kamakura, T. Matsui, J. Kitagawa, Y. Kadoya, Appl. Phys. Lett. 91 (1) (2007) 011102.
[114] D.S. Ponomarev, R.A. Khabibullin, A.E. Yachmenev, I.E. Ilyakov, B.V. Shiskin, R.A. Akhmedzhanov, Semiconductors 51 (4) (2017) 509–513.
[115] D.S. Ponomarev, R.A. Khabibullin, A.E. Yachmenev, I.E. Ilyakov, B.V. Shiskin, R.A. Akhmedzhanov, Int. J. High Speed Electron. Syst. 25 (3–4) (2016) 1640023.
[116] A.E. Yachmenev, R.A. Khabibullin, I.E. Ilyakov, I.A. Glinskiy, A.S. Kucheryavenko, B.V. Shishkin, R.A. Akhmedzhanov, K.I. Zaytsev, D.S. Ponomarev, Proc. SPIE (2018) 108000D.
[117] S.V. Ivanova, M. Yu. Chernova, V.A. Solov'eva, P.N. Brunkova, D.D. Firsov, O.S. Komkov, Prog. Cryst. Growth Charact. Mater. 65 (1) (2019) 20–35.
[118] J.-.S. Hwang, H.-.C. Lin, C.-.K. Chang, T.-.S. Wang, L.-.S. Chang, J.-.I. Chyi, W.-.S. Liu, S.-.H. Chen, H.-.H. Lin, P.-.W. Liu, Opt. Express 15 (2007) 5120–5125.
[119] V. Apostolopoulos, M.E. Barnes, J. Phys. D Appl. Phys. 47 (2014) 374002.
[120] G. Klatt, B. Surrer, D. Stephan, O. Schubert, M. Fischer, J. Faist, A. Leitenstorfer, R. Huber, T. Dekorsy, Appl. Phys. Lett. 98 (2011) 021114.
[121] D. McBryde, M.E. Barnes, A. Berry, P. Gow, H.E. Beere, D.A. Ritchie, V. Apostolopoulos, Opt. Express 22 (3) (2014) 3234–3243.
[122] G. Klatt, F. Hilser, W. Qiao, M. Beck, R. Gebs, A. Bartels, K. Huska, U. Lemmer, G. Bastian, M.B. Johnston, M. Fischer, J. Faist, T. Dekorsy, Opt. Express 18 (5) (2010) 4939–4947.
[123] P. Gow, S.A. Berry, D. McBryde, M.E. Barnes, H.E. Beere, D.A. Ritchie, V. Apostolopoulos, Appl. Phys. Lett. 103 (2013) 252101.
[124] A. Takazato, M. Kamakura, T. Matsui, J. Kitagawa, Y. Kadoya, Appl. Phys. Lett. 90 (10) (2007) 101119.
[125] B. Sartorius, H. Roehle, H. Kunzel, J. Bottcher, M. Schlak, D. Stanze, H. Venghaus, M. Schell, Opt. Express 16 (13) (2008) 9565–9570.
[126] O. Hatem, J. Cunningham, E.H. Linfield, C.D. Wood, G. Davies, P.J. Cannard, M.J. Robertson, D.G. Moodie, Appl. Phys. Lett. 98 (12) (2011) 121107.
[127] B. Globisch, R.J.B. Dietz, R.B. Kohlhaas, T. Gobel, M. Schell, D. Alcer, M. Semtsiv, W.T. Masselink, J. Appl. Phys. 121 (2017) 053102.
[128] M. Suzuki, M. Tonouchi, Appl. Phys. Lett. 86 (2005) 163504.
[129] M. Suzuki, M. Tonouchi, Appl. Phys. Lett. 86 (5) (2005) 051104.
[130] N. Chimot, J. Mangeney, L. Joulaud, P. Crozat, H. Bernas, K. Blary, J.F. Lampin, Appl. Phys. Lett. 87 (19) (2005) 193510.
[131] N. Chimot, J. Mangeney, P. Mounaix, M. Tondusson, K. Blary, J.F. Lampin, Appl. Phys. Lett. 89 (2006) 083519.
[132] I. Beleckaite, J. Treu, S. Morkotter, M. Doblinger, X. Xu, R. Adomavicius, J.J. Finley, G. Koblmuller, A. Krotkus, Appl. Phys. Lett. 110 (2017) 201106.
[133] R. Takahashi, Y. Kawamura, Appl. Phys. Lett. 65 (14) (1994) 1790–1792.
[134] Y. Chen, S.S. Prabhu, S.E. Ralph, D.T. McInturff, Appl. Phys. Lett. 72 (4) (1998) 439.
[135] K. Biermann, D. Nickel, K. Reimann, M. Woerner, T. Elsaesser, H. Kunzel, Appl. Phys. Lett. 80 (11) (2002) 1936.
[136] H. Künzel, J. Böttcher, R. Gibis, G. Urmann, Appl. Phys. Lett. 61 (11) (1992) 1347.
[137] W.-.U. Oh, J.-.E. Oh, S.-.R. Ryoo, S.-.H. Paek, C.-.K. Chung, T.-.W. Kang, J. Appl. Phys. 74 (11) (1993) 7016.
[138] I. Kostakis, D. Saeedkia, M. Missous, J. Appl. Phys. 111 (2012) 103105.
[139] R.J. Dietz, B. Globisch, H. Roehle, D. Stanze, T. Göbel, M. Schell, Opt. Express 22 (2014) 19411.
[140] R.B. Kohlhaas, R.J.B. Dietz, S. Breuer, S. Nellen, L. Liebermeister, M. Schell, B. Globisch, Opt. Lett. 43 (2018) 5423.
[141] T. Göbel, D. Stanze, B. Globisch, R.J.B. Dietz, H. Roehle, M. Schell, Opt. Lett. 38

(2013) 4197.
[142] A.J. Deninger, A. Roggenbuck, S. Schindler, S. Preu, J. Infrared Millim, Terahertz Waves 36 (2015) 269–277.
[143] R.J.B. Dietz, Photoconductive THz Emitters and Detectors On the Basis of InGaAs/InP For Terahertz Time Domain Spectroscopy, Ph.D. thesis Philipps-Universität, Marburg, 2015.
[144] J.F. Zheng, J.D. Walker, M.B. Salmeron, E.R. Weber, Phys. Rev. Lett. 72 (1994) 2414.
[145] Y. Chen, P. Bhattacharya, J. Singh, J. Cryst. Growth 111 (1991) 228–232.
[146] D.C. Driscoll, M. Hanson, C. Kadow, A.C. Gossard, Appl. Phys. Lett. 78 (2001) 1703.
[147] M.P. Hanson, D.C. Driscoll, E. Muller, A.C. Gossard, Physica E Low Dimens. Syst. Nanostruct. 13 (2–4) (2002) 602–605.
[148] D.C. Driscoll, M.P. Hanson, A.C. Gossard, J. Appl. Phys. 97 (2005) 016102.
[149] D.C. Driscoll, M.P. Hanson, A.C. Gossard, E.R. Brown, Appl. Phys. Lett. 86 (2005) 051908.
[150] A. Schwagmann, Z.-.Y. Zhao, F. Ospald, H. Lu, D.C. Driscoll, M.P. Hanson, A.C. Gossard, J.H. Smet, Appl. Phys. Lett. 96 (2010) 141108.
[151] S. Preu, M. Mittendorff, H. Lu, H.B. Weber, S. Winner, A.C. Gossard, Appl. Phys. Lett. 101 (2012) 101105.
[152] N.T. Yardimci, H. Lu, M. Jarrahi, Appl. Phys. Lett. 109 (2016) 191103.
[153] A.D.J. Fernandez Olvera, H. Lu, A.C. Gossard, S. Preu, Opt. Express 25 (2017) 29492–29500.
[154] R. Salas, S. Guchhait, S.D. Sifferman, K.M. McNicholas, V.D. Dasika, E.M. Krivoy, D. Jung, M.L. Lee, S.R. Bank, Appl. Phys. Lett. 106 (2015) 081103.
[155] R. Salas, S. Guchhait, K.M. McNicholas, S.D. Sifferman, V.D. Dasika, D. Jung, E.M. Krivoy, M.L. Lee, S.R. Bank, Appl. Phys. Lett. 108 (2016) 182102.
[156] R. Salas, S. Guchhait, S.D. Sifferman, K.M. McNicholas, V.D. Dasika, D. Jung, E.M. Krivoy, M.L. Lee, S.R. Bank, APL Mater. 5 (2017) 096106.
[157] A. Fekecs, M. Bernier, D. Morris, M. Chicoine, F. Schiettekatte, P. Charette, R. Ares, Opt. Mater. Express 1 (2011) 1165–1177.
[158] F. André, C. Martin, I. Bouraoui, S. François, G.C. Paul, A. Richard, J. Phys. D Appl. Phys. 46 (2013) 165106.
[159] O. Hatem, J.R. FreemanJ. E. Cunningham, P.J. Cannard, M.J. Robertson, E.H. Linfield, A.G. Davies, D.G. Moodie, J. Infrared Millim. Terahertz Waves 37 (2016) 415.
[160] V. Pačebutas, S. Stanionytė, R. Norkus, A. Bičiūnas, A. Urbanowicz, A. Krotkus, J. Appl. Phys. 125 (2019) 174507.
[161] V. Pacebutas, A. Bičiūnas, S. Balakauskas, A. Krotkus, G. Andriukaitis, D. Lorenc, A. Pugžlys, A. Baltuška, Appl. Phys. Lett. 97 (2010) 031111.
[162] L. Xu, X.C. Zhang, D.H. Auston, B. Jalali, Appl. Phys. Lett. 59 (1991) 3357.
[163] L. Xu, B.B. Hu, W. Xin, D.H. Auston, J.D. Morse, Appl. Phys. Lett. 62 (1993) 3507.
[164] W. Sha, A.L. Smirl, W.F. Tseng, Phys. Rev. Lett. 74 (1995) 4273.
[165] R. Kersting, K. Unterrainer, G. Strasser, H.F. Kauffmann, E. Gornik, Phys. Rev. Lett. 79 (1997) 3038.
[166] W. Fischler, P. Buchberger, R.A. Höpfel, G. Zandler, Appl. Phys. Lett. 68 (1996) 2778.
[167] A. Reklaitis, Phys. Rev. B 77 (2008) 153309.
[168] A. Lisauskas, A. Reklaitis, R. Venckevičius, I. Kašalynas, G. Valušis, G. Grigaliūnaitė–Vonsevičienė, H. Maestre, J. Schmidt, V. Blank, M.D. Thomson, H.G. Roskos, K. Köhler, Appl. Phys. Lett. 98 (2011) 091103.
[169] D.J.A. Stohr, R. Heinzelmann, K. Hagedorn, R. Gusten, F. Schafer, H. Stuer, F. Siebe, P. van der Wal, V. Krozer, M. Feiginov, D. Jager, J. Electron. Mater. 37 (2001) 1347–1348.
[170] H. Ito, F. Nakajima, T. Furuta, T. Ishibashi, Semicond. Sci. Technol. 20 (2005) 191.
[171] V. Rymanov, A. Stohr, S. Dulme, T. Tekin, Opt. Express 22 (2014) 7550–7558.
[172] G.H. Döhler, F. Renner, O. Klar, M. Eckardt, A. Schwanhäußer, S. Malzer, D. Driscoll, M. Hanson, A.C. Gossard, G. Loata, T. Löffler, H. Roskos, Semicond. Sci. Technol. 20 (2005) 178.
[173] S. Preu, F.H. Renner, S. Malzer, G.H. Döhler, L.J. Wang, Appl. Phys. Lett. 90 (2007) 212115.
[174] C. Müller-Landau, S. Malzer, H.B. Weber, G.H. Döhler, S. Winnerl, P. Burke, A.C. Gossard, S. Preu, Semicond. Sci. Technol. 33 (2018) 114015.
[175] M. Xu, M. Mittendorff, R.J.B. Dietz, H. Künzel, B. Sartorius, T. Göbel, H. Schneider, M. Helm, S. Winner, Appl. Phys. Lett. 103 (2013) 251114.
[176] L.H. Li, L. Chen, J.R. Freeman, M. Salih, P. Dean, A.G. Davies, E.H. Linfield, Electron. Lett. 53 (12) (2017) 799–800.
[177] X. Wang, C. Shen, T. Jiang, Z. Zhan, Q. Deng, W. Li, W. Wu, N. Yang, W. Chu, S. Duan, AIP Adv. 6 (2016) 075210.
[178] C. Walther, M. Fischer, G. Scalari, R. Terazzi, N. Hoyler, J. Faist, Appl. Phys. Lett. 91 (2007) 131122.
[179] M. Wienold, B. Roben, X. Lu, G. Rozas, L. Schrottke, K. Biermann, H.T. Grahn, Appl. Phys. Lett. 107 (2015) 202101.
[180] M.A. Kainz, M.P. Semtsiv, G. Tsianos, S. Kurlov, W.T. Masselink, S. Schönhuber, H. Detz, W. Schrenk, K. Unterrainer, G. Strasser, A.M. Andrews, Opt. Express 27 (2019) 20688–20693.
[181] J.J. Faist, F. Capasso, D.L. Sivco, C. Sirtori, A.L. Hutchinson, A.Y. Cho, Science 264 (1994) 553–556.
[182] J. Faist, F. Capasso, C. Sirtori, D.L. Sivco, A.Y. Cho, L. Pfeifer, K. West, Solid State Electron. 37 (1994) 1273–1276.
[183] D.V. Ushakov, A.A. Afonenko, A.A. Dubinov, V.I. Gavrilenko, I.S. Vasil'evskii, N.V. Shchavruk, D.S. Ponomarev, R.A. Khabibullin, Quantum Electron. 48 (2018) 1005–1008.
[184] R. Khabibullin, D. Ushakov, A. Afonenko, N. Shchavruk, D. Ponomarev, I. Vasil'evskii, D. Safonov, A. Dubinov, Saratov Fall Meeting 2018: Laser Physics, Photonic Technologies, and Molecular Modeling 11066, 20191106613.
[185] R.A. Khabibullin, N.V. Shchavruk, A.N. Klochkov, I.A. Glinskiy, N.V. Zenchenko, D.S. Ponomarev, P.P. Maltsev, A.A. Zaycev, F.I. Zubov, A.E. Zhukov, G.E. Cirlin, Zh.I. Alferov, Semiconductors 51 (2017) 540–546.
[186] R.A. Khabibullin, N.V. Shchavruk, A. Yu. Pavlov, A.N. Klochkov, D.S. Ponomarev, I.A. Glinskiy, P.P. Maltsev, A.E. Zhukov, G.E. Cirlin, Zh.I. Alferov, Int. J. High Speed Electron. Syst. 25 (2016) 1640022.
[187] C. Deutsch, A. Benz, H. Detz, P. Klang, M. Nobile, A.M. Andrews, W. Schrenk, T. Kubis, P. Vogl, G. Strasser, K. Unterrainer, Appl. Phys. Lett. 97 (2010) 261110.
[188] C. Deutsch, M. Krall, M. Brandstetter, H. Detz, A. Andrews, P. Klang, W. Schrenk, G. Strasser, K. Unterrainer, Appl. Phys. Lett. 101 (2012) 211117.
[189] M. Brandstetter, M.A. Kainz, T. Zederbauer, M. Krall, S. Schonhuber, H. Detz, W. Schrenk, A.M. Andrews, G. Strasser, K. Unterrainer, Appl. Phys. Lett. 108 (2016) 011109.
[190] H. Detz, A.M. Andrews, M.A. Kainz, S. Schönhuber, T. Zederbauer, D. MacFarland, M. Krall, C. Deutsch, M. Brandstetter, P. Klang, W. Schrenk, K. Unterrainer, G. Strasser, Phys. Status Solidi A 216 (2019) 1800504.
[191] H.E. Beere, J.C. Fowler, J. Alton, E.H. Linfield, D.A. Ritchie, R. Köhler, A. Tredicucci, G. Scalari, L. Ajili, J. Faist, S. Barbieri, J. Cryst. Growth 278 (2005) 756–764.
[192] L.L. Chang, K. Ploog, Molecular Beam Epitaxy and Heterostructures, Springer Science & Business Media, 2012.
[193] L.H. Li, J.X. Zhu, L. Chen, A.G. Davies, E.H. Linfield, Opt. Express 23 (2015) 2720–2729.
[194] I.S. Vasil'evskii, A.N. Vinichenko, M.M. Grekhov, V.V. Saraykin, A.N. Klochkov, N. I. Kargin, R.A. Khabibullin, S.S. Pushkarev, EPJ Web Conf. (2018) 04006.
[195] H.E. Beere, D.A. Ritchie, Molecular Beam Epitaxy: Materials and Applications for Electronics and Optoelectronics, Chapter 11. Molecular Beam Epitaxial Growth of Terahertz Quantum Cascade Lasers, John Wiley & Sons, 2019, pp. 175–190.
[196] T. Roch, A.M. Andrews, G. Fasching, A. Benz, W. Schrenk, K. Unterrainer, G. Strasser, Cent. Eur. J. Phys. 5 (2007) 244–251.
[197] R.R. Reznik, N.V. Kryzhanovskaya, F.I. Zubov, A.E. Zhukov, R.A. Khabibullin, S.V. Morozov, G.E. Cirlin, J. Phys. Conf. Ser. 917 (2017) 052012.
[198] S.P. Khanna, S. Chakraborty, M. Lachab, N.M. Hinchcliffe, E.H. Linfield, A.G. Davies, Physica E Low dimens. Syst. Nanostruct 40 (2008) 1859–1861.
[199] S. Gozu, T. Mozume, H. Kuwatsuka, H. Ishikawa, Nanoscale Res. Lett. 7 (2012) 620.
[200] K. Leosson, J.R. Jensen, W. Langbein, J.M. Hvam, Phys. Rev. B 61 (2000) 10322–10329.
[201] Y.V. Flores, A. Albo, IEEE J. Quantum Electron. 53 (2017) 1–8.
[202] N. Linh Tran, G. Biasiol, A. Jollivet, A. Bertocci, F.H. Julien, J.-.M. Manceau, R. Colombelli, Photonics 6 (2019) 38.
[203] C.A. Wang, B. Schwarz, D.F. Siriani, M.K. Connors, L.J. Missaggia, D.R. Calawa, D. McNulty, A. Akey, M.C. Zheng, J.P. Donnelly, T.S. Mansuripur, F. Capasso, J. Cryst. Growth 464 (2017) 215.
[204] A.V. Ikonnikov, K.V. Marem'yanin, S.V. Morozov, V.I. Gavrilenko, A.Yu. Pavlov, N.V. Shchavruk, R.A. Khabibullin, R.R. Reznik, G.E. Cirlin, F.I. Zubov, A.E. Zhukov, Zh.I. Alferov, Tech. Phys. Lett. 43 (2017) 362–365.
[205] X. Lü, E. Luna, L. Schrottke, K. Biermann, H.T. Grahn, Appl. Phys. Lett. 113 (2018) 172101.
[206] G. Scalari, L. Ajili, J. Faist, H. Beere, E. Linfield, D. Ritchie, G. Davies, Appl. Phys. Lett. 82 (2003) 3165–3167.
[207] B.S. Williams, H. Callebaut, S. Kumar, Q. Hu, J.L. Reno, Appl. Phys. Lett. 82 (2003) 1015–1017.
[208] S. Kumar, C.W.I. Chan, Q. Hu, J.L. Reno, Nature Phys. 7 (2011) 166–171.
[209] B.S. Williams, Nature photon. 1 (2007) 517.
[210] S. Kumar, IEEE J. Sel. Top. Quantum Electron. 17 (2010) 38–47.
[211] G. Liang, T. Liu, Q.J. Wang, IEEE J. Sel. Top. Quantum Electron 23 (2016) 1–18.
[212] H.E. Beere, C.H. Worrall, S. Whelan, D.A. Ritchie, J. Alton, S. Barbieri, C. Sirtori, J. Cryst. Growth 301-302 (2007) 935–940.
[213] J.R. Freeman, Heterogeneous Terahertz Quantum Cascade Lasers, Ph.D. thesis University of Cambridge, 2009.
[214] P. Dean, N.K. Saat, S.P. Khanna, M. Salih, A. Burnett, J. Cunningham, E.H. Linfield, A.G. Davies, Opt. Express 17 (2009) 20631–20641.
[215] L. Ajili, G. Scalari, M. Giovannini, N. Hoyler, J. Faist, J. Appl. Phys. 100 (2006) 043102.
[216] D. Bana, M. Wachter, H.C. Liu, Z.R. Wasilewski, M. Buchanan, G.C. Aers, J. Vac. Sci. Technol. A 24 (2006) 778–782.
[217] M.I. Amanti, G. Scalari, R. Terazzi, M. Fischer, M. Beck, J. Faist, A. Rudra, P. Gallo, E. Kapon, New J. Phys. 11 (2009) 125022.
[218] C. Deutsch, H. Detz, M. Krall, M. Brandstetter, T. Zederbauer, A.M. Andrews, W. Schrenk, G. Strasser, K. Unterrainer, Appl. Phys. Lett. 102 (2013) 201102.
[219] A. Albo, Q. Hu, Appl. Phys. Lett. 107 (2015) 241101.
[220] M. Wienold, L. Schrottke, M. Giehler, R. Hey, W. Anders, H.T. Grahn, Appl. Phys. Lett. 97 (2010) 071113.
[221] M.A. Kainz, Schonhuber S, A.M. Andrews, H. Detz, B. Limbacher, G. Strasser, K. Unterrainer, ACS Photonics 5 (2018) 4687–4693.
[222] L. Schrottke, X. Lu, G. Rozas, K. Biermann, H.T. Grahn, Appl. Phys. Lett. 108 (2016) 102102.
[223] L. Gao, J.L. Reno, S. Kumar, Photonics 7 (2020) 7.
[224] D. Turcinkova, G. Scalari, F. Castellano, M.I. Amanti, M. Beck, J. Faist, Appl. Phys. Lett. 99 (2011) 191104.
[225] M. Rosch, G. Scalari, M. Beck, J. Faist, Nature Photon. 9 (2015) 42.
[226] S.A. Diddams, D.J. Jones, J. Ye, S.T. Cundiff, J.L. Hall, J.K. Ranka, R.S. Windeler, R. Holzwarth, T. Udem, T.W. Hansch, Phys. Rev. Lett. 84 (2000) 5102–5105.
[227] A. Forrer, M. Rosch, M. Singleton, M. Beck, J. Faist, G. Scalari, Opt. Express 26 (2018) 23167–23177.

[228] D. Bachmann, N. Leder, M. Rösch, G. Scalari, M. Beck, H. Arthaber, J. Faist, K. Unterrainer, J. Darmo, Opt. Express 23 (2015) 3117–3125.
[229] S. Suzuki, A. Teranishi, K. Hinata, M. Asada, H. Sugiyama, H. Yokoyama, Appl. Phys. Express 2 (2009) 054501.
[230] J.S. Scott, J.P. Kaminski, M. Wanke, S.J. Allen, D.H. Chow, M. Lui, T.Y. Liu, Appl. Phys. Lett. 64 (1994) 1995.
[231] M. Feiginov, J. Infrared Millim, Terahertz Waves 40 (2019) 365.
[232] M. Asada, S. Suzuki, N. Kishimoto, Jpn. J. Appl. Phys. 47 (6) (2008) 4375.
[233] M. Asada, S. Suzuki, T. Fukuma, AIP Adv. 7 (2017) 115226.
[234] K.J.P. Jacobs, B.J. Stevens, R. Baba, O. Wada, T. Mukai, R.A. Hogg, AIP Adv. 7 (2017) 105316.
[235] R. Sekiguchi, Y. Koyama, T. Ouchi, Appl. Phys. Lett. 96 (2010) 062115.
[236] S. Suzuki, M. Asada, A. Teranishi, H. Sugiyama, H. Yokoyama, Appl. Phys. Lett. 97 (2010) 242102.
[237] M. Feiginov, C. Sydlo, O. Cojocari, P. Meissner, Appl. Phys. Lett. 99 (2011) 233506.
[238] H. Kanaya, H. Shibayama, R. Sogabe, S. Suzuki, M. Asada, Appl. Phys. Express 5 (2012) 124101.
[239] Y. Koyama, R. Sekiguchi, T. Ouchi, Appl. Phys. Express 6 (2013) 064102.
[240] H. Kanaya, R. Sogabe, T. Maekawa, S. Suzuki, M. Asada, J. Infrared Millim, Terahertz Waves 35 (2014) 425.
[241] T. Maekawa, H. Kanaya, S. Suzuki, M. Asada, Electron. Lett. 50 (17) (2014) 1214.
[242] H. Kanaya, T. Maekawa, S. Suzuki, M. Asada, Jap. J. Appl. Phys. 54 (2015) 094103.
[243] J. Lee, M. Kim, K. Yang, IEEE Trans. Terahertz Sci. Technol. 6 (2016) 336.
[244] T. Nakagawa, H. Imamoto, T. Kojima, K. Ohta, Appl. Phys. Lett. 49 (1986) 73.
[245] L. Esaki, R. Tsu, IBM J. Res. Develop. 14 (1) (1970) 61–65.
[246] J. Grenzer, A.A. Ignatov, E. Schomburg, K.F. Renk, D.G. Pavel'ev, Yu. Koschurinov, B. Melzer, S. Ivanov, S. Schaposchnikov, P.S. Kop'ev, Ann. Phys. 507 (3) (1995) 184–190.
[247] S. Winner, S. Pesah, E. Schomburg, J. Grenzer, K.F. Renk, H.P.M. Pellemans, A.F.G. Van der Meer, D.G. Pavel'ev, Y.U. Koschurinov, A.A. Ignatov, B. Melzer, V. Ustinov, S. Ivanov, P.S. Kop'ev, Superlattices Microst. 25 (1/2) (1999) 57.
[248] D.G. Pavel'ev, N.V. Demarina, Yu.I. Koshurinov, A.P. Vasil'ev, E.S. Semenova, A.E. Zhukov, V.M. Ustinov, Semiconductors 38 (2004) 1105.
[249] C.P. Endres, F. Lewen, T.F. Giesen, S. Schlemmer, D.G. Paveliev, Y.I. Koschurinov, V.M. Ustinov, A.E. Zhucov, Rev. Sci. Instrum. 78 (2007) 043106.
[250] H. Eisele, I. Farrer, E.H. Linfield, D.A. Ritchie, Appl. Phys. Lett. 93 (2008) 182105.
[251] D.G. Paveliev, Y.I. Koshurinov, A.S. Ivanov, A.N. Panin, V.L. Vax, V.I. Gavrilenko, A.V. Antonov, V.M. Ustinov, A.E. Zhukov, Semiconductors 46 (1) (2012) 121.
[252] H. Eisele, L. Li, E.H. Linfield, Appl. Phys. Lett. 112 (2018) 172103.
[253] A. Apostolakis, M.F. Pereira, AIP Adv. 9 (2019) 015022.
[254] A.A. Andronov, M.N. Drozdov, D.I. Zinchenko, A.A. Marmalyuk, I.M. Nefedov, Yu.N. Nozdrin, A.A. Padalitsa, A.V. Sosnin, A.V. Ustinov, V.I. Shashkin, Phys. Usp. 46 (2003) 755.
[255] T. Unuma, N. Sekine, K. Hirakawa, AIP Conf. Proc. 893 (2007) 495.
[256] A. Naka, K. Hirakawa, T. Unuma, Appl. Phys. Express 9 (2016) 112101.
[257] T. Unuma, A. Matsuda, Appl. Phys. Lett. 112 (2018) 162107.